Article

Higher-order protein assembly controls kinetochore formation

Gunter B. Sissoko[1,2,4], Ekaterina V. Tarasovetc[3,4], Océane Marescal[1,2], Ekaterina L. Grishchuk [3] ✉ & Iain M. Cheeseman [1,2] ✉

To faithfully segregate chromosomes during vertebrate mitosis, kinetochore–microtubule interactions must be restricted to a single site on each chromosome. Prior work on pair-wise kinetochore protein interactions has been unable to identify the mechanisms that prevent outer kinetochore formation in regions with a low density of CENP-A nucleosomes. To investigate the impact of higher-order assembly on kinetochore formation, we generated oligomers of the inner kinetochore protein CENP-T using two distinct, genetically engineered systems in human cells. Although individual CENP-T molecules interact poorly with outer kinetochore proteins, oligomers that mimic centromeric CENP-T density trigger the robust formation of functional, cytoplasmic kinetochore-like particles. Both in cells and in vitro, each molecule of oligomerized CENP-T recruits substantially higher levels of outer kinetochore components than monomeric CENP-T molecules. Our work suggests that the density dependence of CENP-T restricts outer kinetochore recruitment to centromeres, where densely packed CENP-A recruits a high local concentration of inner kinetochore proteins.

The kinetochore is the essential protein complex that tethers condensed chromosomes to spindle microtubules during mitosis[1,2]. Individual kinetochore components and subcomplexes have been studied extensively. However, metazoan kinetochores are higher-order assemblies composed over 100 components and hundreds of copies of each component[2–7]. Because our current understanding of kinetochore formation is based on simplified biochemical systems and pair-wise interactions, the role of kinetochore high-order assembly remains unclear. Like kinetochores components, a growing number of proteins are recognized as components of higher-order assemblies with large or undefined stoichiometries[8–10]. Recent work suggests that incorporation into higher-order assemblies spatially regulates the activities of these proteins[8,10–12]. Higher-order assemblies locally concentrate macromolecules, enabling reactions and interactions within the assemblies that do not occur at whole-cell concentrations. As the location and number of kinetochores on each chromosome are critical to ensuring proper chromosome segregation and avoiding DNA damage, we hypothesized

that the spatial regulation conferred by higher-order assembly could act in kinetochore formation.

The kinetochore is composed of two regions whose assembly mechanisms are tightly controlled in cells. The inner kinetochore is the subset of kinetochore proteins that resides at centromeric DNA throughout the cell cycle[13]. Upon mitotic entry, the inner kinetochore recruits outer kinetochore proteins[13–19], which perform the kinetochore's mechanical and signalling functions[2]. Kinetochore formation is restricted to a single site on each chromosome called the centromere[1,2]. Additional sites of kinetochore formation result in aberrant chromosome–microtubule interactions that cause DNA damage and chromosome segregation errors[20–22]. To direct kinetochore components to centromeres, vertebrate cells mark these regions epigenetically with the histone H3 variant CENP-A[23]. Although CENP-A nucleosomes are necessary to specify the site of kinetochore formation, CENP-A does not drive complete outer kinetochore recruitment when it is dispersed on chromosome arms[21,24]. Similarly, although

[1]Whitehead Institute for Biomedical Research, Cambridge, MA, USA. [2]Department of Biology, Massachusetts Institute of Technology, Cambridge, MA, USA. [3]Department of Physiology, Perelman School of Medicine, University of Pennsylvania, Philadelphia, PA, USA. [4]These authors contributed equally: Gunter B. Sissoko, Ekaterina V. Tarasovetc. ✉e-mail: gekate@pennmedicine.upenn.edu; icheese@wi.mit.edu

complexes of kinetochore proteins can be reconstituted from recombinant proteins in vitro[25–28], kinetochores do not assemble spontaneously in the cytosol[29]. The mechanisms that act alongside CENP-A localization to restrict kinetochore recruitment to centromeres remain unknown. In this Article, we investigate how human cells confine outer kinetochore recruitment to centromere-localized inner kinetochore assemblies using the emergent properties conferred by higher-order assembly.

In vertebrate cells, two distinct pathways recruit the outer kinetochore downstream of CENP-A. In one pathway, the inner kinetochore scaffold CENP-C recruits the outer kinetochore complex MIS12 (refs. 2,30). In turn, MIS12 recruits the KNL1 complex and the NDC80 complex[2,31]. In the second pathway, the inner kinetochore protein CENP-T directly recruits two NDC80 complexes and one MIS12 complex[15,18,19,21]. The relative importance of these two pathways varies dramatically between species[32], but prior work in chicken and human cells has shown that CENP-T is the dominant outer kinetochore assembly factor in vertebrates[6,16,32,33]. CENP-T has a structured C-terminal kinetochore localization domain and a disordered N-terminal region with multiple binding sites for outer kinetochore proteins (Fig. 1a)[15,18,19,21,34]. CENP-T is clustered at kinetochores, with approximately 72 copies per human kinetochore[3]. Although CENP-T has no known oligomerization domain, higher-order assembly of the entire inner kinetochore brings CENP-T to a high local concentration[2,3,5,6].

Here, we mimic the high local concentration of CENP-T at centromeres using artificial oligomerization systems. With this approach, we demonstrate that oligomerizing the N-terminal region of CENP-T is sufficient to trigger outer kinetochore recruitment and generate kinetochore-like particles in the cytoplasm.

Results

CENP-T oligomers form kinetochore-like particles

To study the role of higher-order assembly in CENP-T function, we artificially oligomerized a 242 amino acid region of the CENP-T N-terminus (CENP-T$^{1–242}$). This region contains binding sites for the outer kinetochore complexes NDC80 and MIS12 but lacks CENP-T's kinetochore localization domain[2,15,19,21,25,34]. We fused GFP–CENP-T$^{1–242}$ to I3-01, a 22 kDa oligomerizing tag that forms a 60-subunit homo-oligomer[35] (GFP–CENP-T$^{1–242}$–I3-01; Fig. 1a). In interphase HeLa cells, GFP–CENP-T$^{1–242}$–I3-01 and GFP–I3-01 control oligomers formed puncta throughout the cytoplasm, consistent with oligomer formation (Fig. 1b). In cells with high expression levels, we also observed larger foci, which may indicate that some oligomers form larger aggregates. In mitotic cells, GFP–CENP-T$^{1–242}$–I3-01 localized to spindle poles and spindle microtubules, whereas GFP–I3-01 control oligomers localized throughout the cytoplasm (Fig. 1c,d). GFP–CENP-T$^{1–242}$–I3-01 also appeared to cause severe mitotic defects that we will address later.

Because CENP-T itself does not bind to microtubules, we tested whether GFP–CENP-T$^{1–242}$–I3-01 recruited microtubule-binding outer kinetochore components. Using immunofluorescence, we found that NDC80, the kinetochore's primary microtubule receptor, co-localized with GFP–CENP-T$^{1–242}$–I3-01 (Fig. 2a, b). GFP–CENP-T$^{1–242}$–I3-01 also recruited the core outer kinetochore complexes MIS12 and KNL1 (Fig. 2a,b). By contrast, the inner kinetochore protein CENP-A did not co-localize with GFP–CENP-T$^{1–242}$–I3-01 (Extended Data Fig. 1a,b), consistent with prior findings that the CENP-T N-terminus does not interact with inner kinetochore proteins[21,34,36]. To verify these results independently, we immunoprecipitated GFP–CENP-T$^{1–242}$–I3-01 from mitotic HeLa cells. By mass spectrometry, we confirmed that the NDC80, MIS12 and KNL1 complexes interact with GFP–CENP-T$^{1–242}$ oligomers (Fig. 2c). GFP–I3-01 oligomers did not interact with kinetochore proteins in immunofluorescence or mass spectrometry experiments (Fig. 2a,b and Extended Data Fig. 2a). Consistent with our immunofluorescence results, inner kinetochore proteins were not detected or were detected at low levels (Extended Data Fig. 2b).

Endogenous kinetochores also recruit numerous peripheral outer kinetochore-associated proteins[7,37–39]. Among these, the RZZ complex component ZW10 and the SKA1 complex component Ska3 co-localized and co-immunoprecipitated with GFP–CENP-T$^{1–242}$–I3-01 (Fig. 2c and Extended Data Fig. 1a,b). Several other kinetochore-associated proteins, including components of the spindle assembly checkpoint, also co-immunoprecipitated with GFP–CENP-T$^{1–242}$–I3-01 (Fig. 2c). These results suggest that CENP-T$^{1–242}$ recruits a similar set of outer kinetochore components to endogenous kinetochores when oligomerized, generating kinetochore-like particles in the cytoplasm.

CENP-T oligomers are functionally similar to kinetochores

Lateral and end-on attachments to microtubules enable kinetochores to move processively along microtubules and to track depolymerizing and polymerizing microtubule plus-ends[1,38,40,41]. We sought to determine whether GFP–CENP-T$^{1–242}$–I3-01 particles retained these kinetochore functions.

To verify that GFP–CENP-T$^{1–242}$–I3-01 particles interact with microtubules, we isolated GFP–CENP-T$^{1–242}$–I3-01 from mitotic HeLa cells (Fig. 3a and Extended Data Fig. 3a). Based on the fluorescence intensity of the purified oligomers, they contained 41 ± 5 GFP molecules (Fig. 3b and Extended Data Fig. 3b,c). When incubated with stabilized microtubules in vitro, many of the oligomers interacted with microtubule walls (Fig. 3c,d). Using immunofluorescence, we confirmed that the microtubule-bound oligomers had co-purified with the NDC80 complex (Extended Data Fig. 3d), which probably mediated their microtubule interactions[2,42]. Control oligomers did not bind microtubules (Fig. 3c,d).

Next, we introduced the purified oligomers into chambers containing dynamic microtubules (Fig. 3e). Microtubule-bound GFP–CENP-T$^{1–242}$ oligomers exhibited several modes of motility. Some oligomers were captured by growing microtubule plus-ends and moved processively with the elongating ends at the rate of tubulin assembly (Fig. 3f top, 3g, Extended Data Fig. 3e and Supplementary Video 1). Others bound to microtubule walls, then remained stationary or moved processively towards the plus-end at 2.7 ± 0.5 µm min^{-1} ($n = 8$), a rate that is comparable to that of chromosome congression[43] (Extended Data Fig. 3e and Supplementary Video 2). Many microtubule-bound CENP-T$^{1–242}$ oligomers also diffused along the microtubules. Upon encountering a depolymerizing end, these oligomers travelled with the end toward the microtubule seed (Fig. 3f bottom, Extended Data Fig. 3e and Supplementary Video 3). Oligomer-bound ends shortened at half of the rate of oligomer-free ends (Fig. 3g). Previous work suggests that mammalian chromosomes and recombinant assemblies of kinetochore proteins cause a similar suppression of microtubule depolymerization[44,45]. Together, these results suggest that CENP-T$^{1–242}$ oligomers recruit outer kinetochore structures that interact with microtubules similarly to endogenous kinetochores.

CENP-T oligomerization promotes kinetochore assembly

The ability of GFP–CENP-T$^{1–242}$ oligomers to form kinetochore-like particles in the cytoplasm is surprising because we previously found virtually no interactions between soluble CENP-T and the NDC80 complex in mitotic HeLa extract[29]. To investigate how oligomers differ from monomers, we compared the behaviours of GFP–CENP-T$^{1–242}$–I3-01 oligomers with identical constructs lacking an oligomerizing tag (GFP–CENP-T$^{1–242}$). Unlike CENP-T$^{1–242}$ oligomers, which localized almost exclusively to mitotic spindles, GFP–CENP-T$^{1–242}$ monomers localized throughout the cytoplasm of mitotic cells with a modest enrichment on the spindle (Fig. 4a). Quantification confirmed that both constructs co-localized with tubulin, but 95% of GFP–CENP-T$^{1–242}$ oligomer signal overlapped with α-tubulin signal, whereas only 55% of monomer signal overlapped with α-tubulin signal (Fig. 4a and Extended Data Fig. 4a). The more robust spindle localization of CENP-T oligomers could reflect increased microtubule-binding avidity relative to monomers or
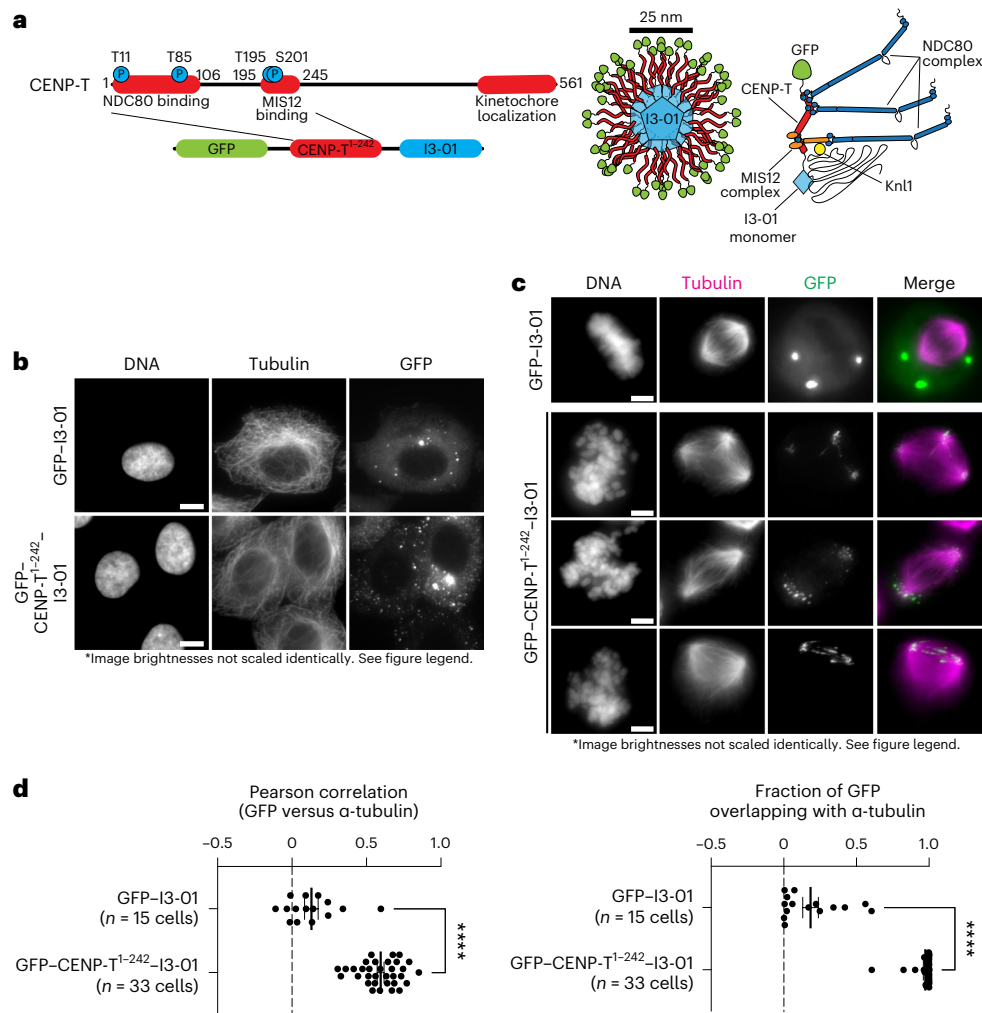
Fig. 1 | I3-01 oligomerization strategy generates particles that interact with mitotic spindles. a, Left top: diagram of endogenous CENP-T, its key phosphorylation sites, and the sites of established interactions. Left bottom: construct used to generate CENP-T$^{1-242}$ oligomers in cells. Right: diagrams of the expected oligomers and their predicted interactions with the outer kinetochore. **b**, Representative images of CENP-T$^{1-242}$ oligomers and control GFP oligomers in interphase HeLa cells. Scale bar, 10 μm. Image brightness is not scaled identically to make the appearance and localization of constructs visible despite large differences in brightness. This experiment was repeated seven times with similar results. **c**, Representative image of control GFP oligomers and examples

of CENP-T$^{1-242}$ oligomers in mitotic HeLa cells. Scale bar, 5 μm. As in **b**, image brightnesses are not scaled identically. This experiment was repeated seven times with similar results. **d**, Pearson correlation and Manders overlap coefficient for GFP and α-tubulin co-localization in cells expressing GFP–I3-01 or GFP–CENP-T$^{1-242}$–I3-01. Each point is a biologically independent cell; *n*, number of cells measured in a single experiment. Bars represent mean ± s.e.m. Each experiment was performed two times with similar results. Two-tailed Welch's *t*-tests: Pearson correlation: *P* < 0.0001; overlap: *P* < 0.0001. Statistical analysis of replicates and source numerical data are available in Source data.

improved outer kinetochore recruitment when GFP–CENP-T$^{1-242}$ is oligomerized[45,46]. If the latter were true, we predicted that GFP–CENP-T$^{1-242}$ oligomers would compete more effectively with endogenous kinetochores for outer kinetochore components than monomers expressed at comparable levels, resulting in distinct phenotypes.

To test how GFP–CENP-T$^{1-242}$ expression impacted endogenous kinetochores, we measured the localization of outer kinetochore complexes to centromeres in mitotic cells expressing GFP–CENP-T$^{1-242}$ monomers, GFP–CENP-T$^{1-242}$ oligomers or GFP control oligomers. Expression of monomeric GFP–CENP-T$^{1-242}$ only moderately reduced NDC80 levels at centromeres compared with control cells expressing GFP oligomers. By contrast, expression of comparable levels of GFP–CENP-T$^{1-242}$–I3-01 severely depleted outer kinetochore proteins from endogenous kinetochores. This was particularly true for the NDC80 complex, which was reduced to 3.7% of control levels (Fig. 4b,c and Extended Data Fig. 4b,c). The total levels of NDC80 in cells expressing GFP–CENP-T$^{1-242}$ oligomers were equal to or greater than the levels in

control cells, so the depletion of the complex from centromeres cannot be explained by a reduction in total levels and is probably due to their sequestration by GFP–CENP-T$^{1-242}$ oligomers (Extended Data Fig. 4d).

Recruitment of the outer kinetochore to exogenous CENP-T oligomers and the resulting depletion of kinetochore proteins from endogenous kinetochores had a dramatic effect on mitotic progression. Expression of monomeric GFP–CENP-T$^{1-242}$ caused only a small increase in the rate of mitotic defects, whereas similar expression levels of GFP–CENP-T$^{1-242}$–I3-01 led to scattered chromosomes and spindle abnormalities in 99% of cells and a potent mitotic arrest (Fig. 4d–f and Extended Data Fig. 4b,c). After 24 h of GFP–CENP-T$^{1-242}$–I3-01 expression, the fraction of cells in G2/M increased from 6.7% to 64.5% based on DNA content analysis, whereas monomeric GFP–CENP-T$^{1-242}$ expression had no impact on the fraction of cells in G2/M (Fig. 4f). The systemic impacts of GFP–CENP-T$^{1-242}$ oligomerization on cells suggest that high density enables CENP-T N-termini to recruit and sequester the outer kinetochore components more efficiently.
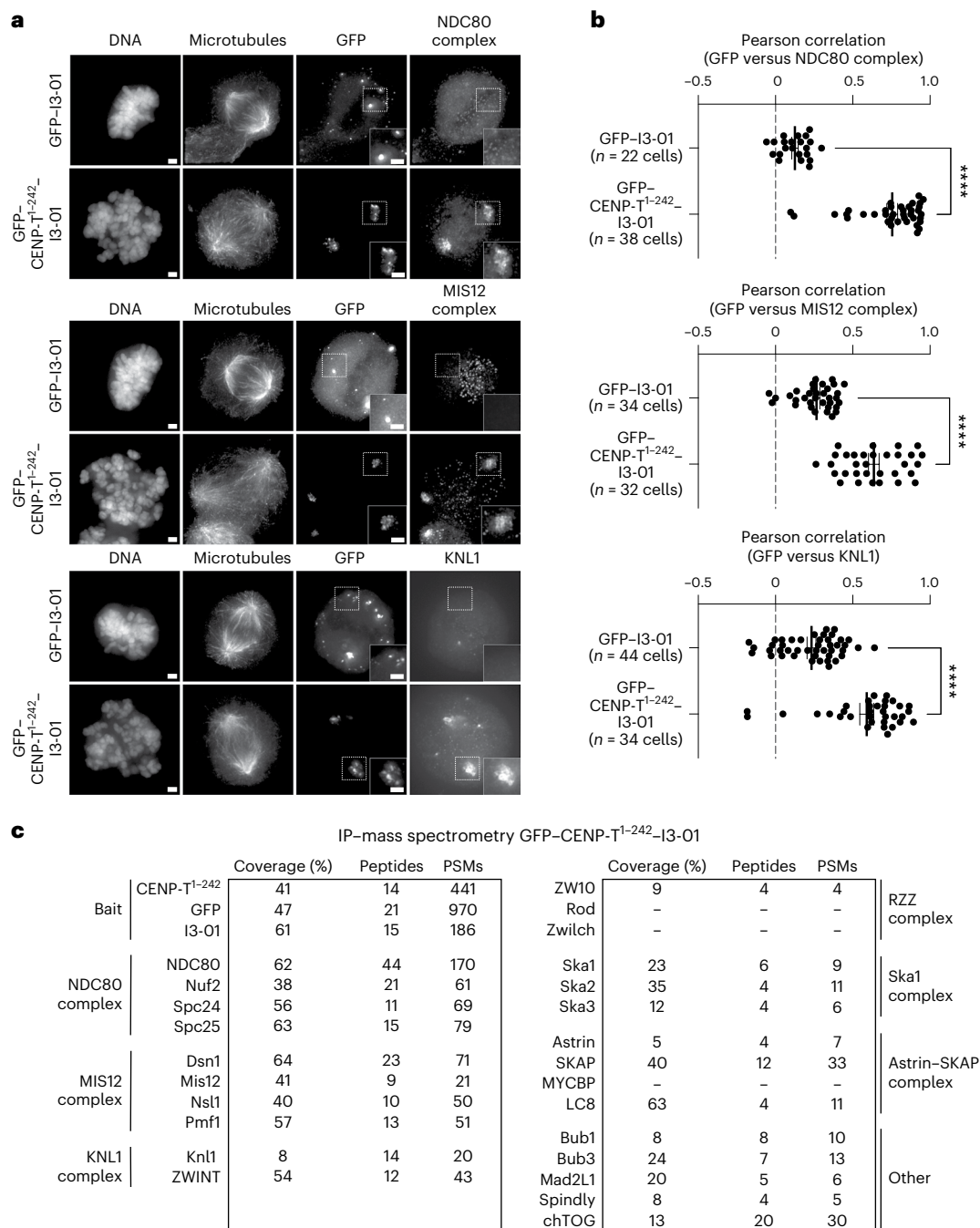
Fig. 2 | CENP-T$^{1-242}$ oligomers recruit almost the entire outer kinetochore.
a, Representative immunofluorescence images of co-localization of outer kinetochore proteins with GFP–CENP-T$^{1-242}$–I3-01 oligomers and GFP–I3-01 controls. Identical linear brightness adjustments were used for GFP and kinetochore protein channels for each pair of experimental and control samples. Regions enlarged in insets are indicated by dashed boxes. Scale bar, 5 μm. These experiments were repeated five times with similar results. **b**, Pearson correlations for the co-localization between GFP and outer kinetochore signals

for GFP–I3-01 and GFP–CENP-T$^{1-242}$–I3-01. Each point is a cell; n, number of cells measured in a single experiment. Each experiment was performed two times with similar results. Bars represent mean ± s.e.m. P values were calculated with two-tailed Welch's t-tests: ****P < 0.0001. **c**, Outer kinetochore and outer kinetochore-associated proteins detected in immunoprecipitation (IP)–mass spectrometry of GFP–CENP-T$^{1-242}$–I3-01. This experiment was performed twice with similar results.

To measure each construct's outer kinetochore recruitment directly, we immunoprecipitated each construct from mitotic HeLa cells, and compared the abundances of interacting partners using quantitative mass spectrometry. To enable a direct comparison of outer kinetochore proteins recruited per CENP-T molecule, we normalized all protein abundances to the abundance of peptides shared between pairs of bait proteins (Methods). Using this approach, we determined that monomeric GFP–CENP-T$^{1-242}$ co-purified with more NDC80

complex and MIS12 complex than the GFP–I3-01 control (Fig. 4g), but GFP–CENP-T$^{1-242}$–I3-01 oligomers associated with 5.6-fold more NDC80 complex, 5.4-fold more MIS12 complex and 2.7-fold more KNL1 complex per CENP-T molecule than monomeric GFP–CENP-T$^{1-242}$ (Fig. 4h and Extended Data Fig. 5a). Furthermore, GFP–CENP-T$^{1-242}$–I3-01 recruited higher levels of downstream kinetochore-associated proteins such as the SKA1 complex, the RZZ complex, Spindly, Mad2L1 and chTOG (Fig. 4h and Extended Data Fig. 5a–c). Thus, monomeric
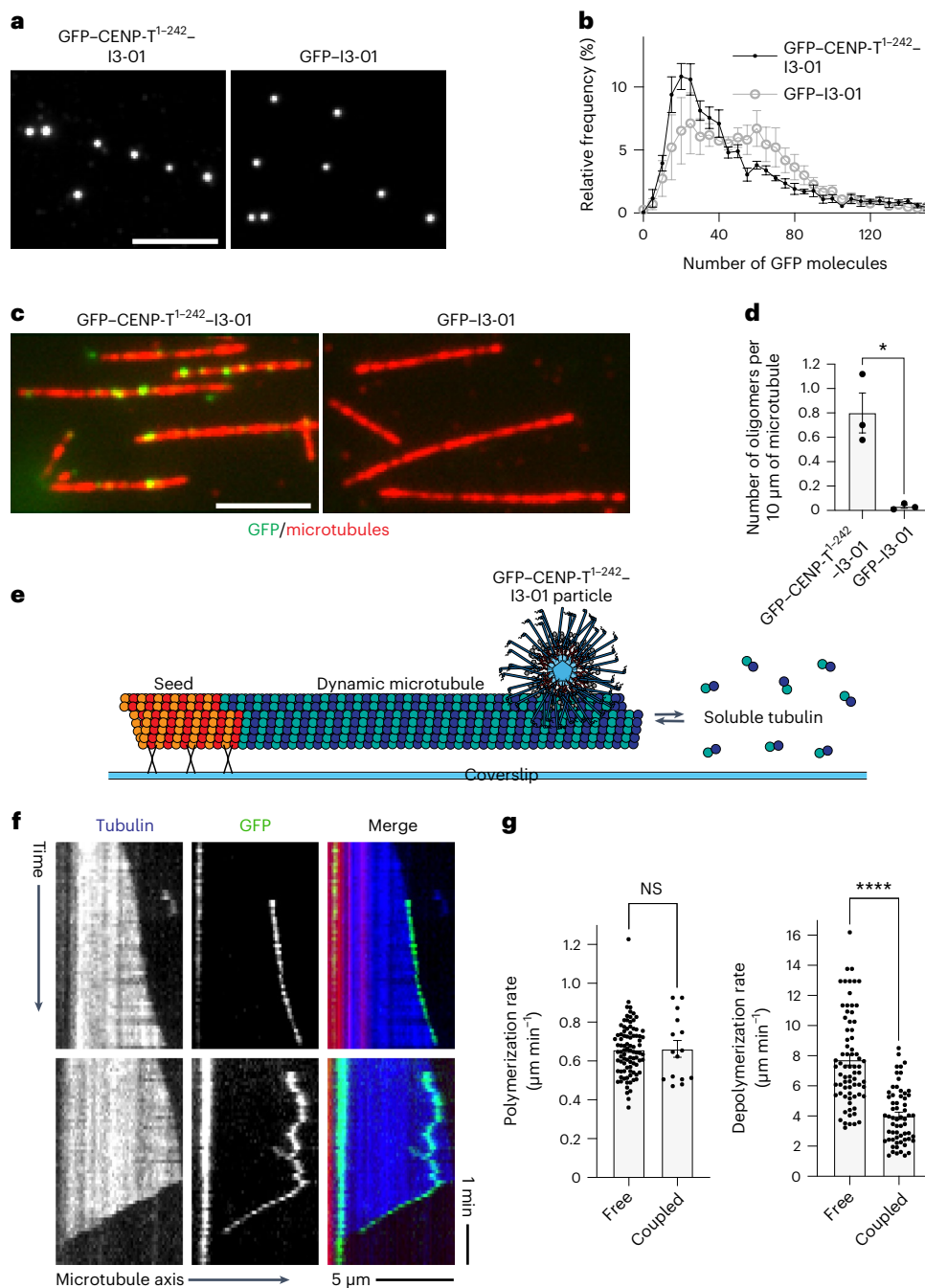
Fig. 3 | Isolated CENP-T$^{1-242}$ oligomers bind to microtubules and track dynamic microtubule ends. a, Representative images of GFP–CENP-T$^{1-242}$–I3-01 and GFP–I3-01 isolated from mitotic cells. Scale bar, 5 μm. Repeated five times with similar results. **b**, Histogram showing the distribution of the number of molecules in each oligomer plotted as a percentage of the total number observed of oligomers. Each point represents mean ± s.e.m. from five independent experiments, in which more than 180 oligomers were analysed. Control oligomers contained 51 ± 8 GFP molecules. **c**, Representative images of fluorescent microtubules (red) incubated with GFP-tagged CENP-T$^{1-242}$ oligomers and control GFP oligomers (green). Scale bar, 5 μm. Repeated three times with similar results. **d**, Average number of microtubule-bound oligomers in a 10 μm length of microtubule. Bars represent mean ± s.e.m. from three independent experiments. Each point represents the mean of an independent experiment in which at least ten microscopy fields were analysed. Two-tailed Welch's *t*-test: *P* = 0.0418. **e**, Schematic of the in vitro assay used to study interactions between CENP-T$^{1-242}$ oligomers and dynamic microtubules. **f**, Representative

kymographs of dynamic microtubules (tubulin, blue in merge) grown from coverslip-bound microtubule seeds (red in merge) and CENP-T$^{1-242}$ oligomers (GFP, green in merge). Top: CENP-T$^{1-242}$ oligomer binds directly to polymerizing microtubule end, then tracks the end during polymerization. Bottom: CENP-T$^{1-242}$ oligomer binds the wall of a microtubule, diffuses on the microtubule lattice and then tracks the depolymerizing microtubule end. End tracking during polymerization and depolymerization were observed in 20 and 63 out of 80 total observations, respectively. Observations were made over eight independent experiments. **g**, Polymerization and depolymerization rates measured for free microtubule ends and microtubule ends coupled to CENP-T$^{1-242}$ oligomers. Points represent individual microtubule ends pooled from three experiments without GFP–CENP-T$^{1-242}$–I3-01 and eight experiments with GFP–CENP-T$^{1-242}$–I3-01. Polymerization rate: *n* = 89 free ends, *n* = 15 coupled ends; depolymerization rate: *n* = 73 free ends, *n* = 62 coupled ends. Bars show the mean ± s.e.m. Two-tailed Welch's *t*-tests: polymerization rate: *P* = 0.9377; depolymerization rate: *P* < 0.0001. NS, not significant.

CENP-T molecules interact weakly with outer kinetochore proteins, but each molecule recruits outer kinetochore proteins more efficiently when oligomerized.

CENP-T activity increases incrementally with oligomer size

The ability of artificial GFP–CENP-T$^{1–242}$–I3-01 oligomers to compete with endogenous kinetochores and produce kinetochore-like particles strongly suggests that high local concentrations of CENP-T activate outer kinetochore recruitment. To determine whether the oligomerization-dependent recruitment has an oligomer size threshold or gradually activates as GFP–CENP-T$^{1–242}$ oligomer size increases, we used an unrelated strategy called the 'SunTag' to manipulate the stoichiometry of CENP-T$^{1–242}$ oligomers[47]. The SunTag is a two-component system with a single-chain monoclonal antibody (scFv), which we fused to CENP-T$^{1–242}$ (scFv–sfGFP–CENP-T$^{1–242}$), and a scaffold with repeats of the antibody's cognate epitope (GCN4pep; Fig. 5a). When scFv–sfGFP–CENP-T$^{1–242}$ is co-expressed with the scaffold, one copy of the scFv–sfGFP–CENP-T$^{1–242}$ fusion protein binds to each GCN4pep repeat, resulting in oligomers of defined sizes[47] (Fig. 5a). We ensured similar scFv–sfGFP–CENP-T$^{1–242}$ expression levels by generating all GCN4pep scaffold-expressing cell lines from the same scFv–sfGFP–CENP-T$^{1–242}$-expressing parental line (Extended Data Fig. 6a–d).

When co-expressed with a single GCN4pep repeat (1xGCN4pep), scFv–sfGFP–CENP-T$^{1–242}$ did not localize robustly to the mitotic spindle. As we increased the number of GCN4pep repeats, we observed mitotic abnormalities and sfGFP–scFv–CENP-T$^{1–242}$ began to localize to spindle poles (Fig. 5b). With six or more GCN4pep repeats, sfGFP–scFv–CENP-T$^{1–242}$ robustly localized to spindle poles and spindle microtubules (Fig. 5b), like GFP–CENP-T$^{1–242}$–I3-01 kinetochore particles. Similarly, scFv–sfGFP–CENP-T$^{1–242}$ expression with 1xGCN4pep or 2xGCN4pep did not cause a cell cycle arrest, but the fraction of cells in G2/M increased gradually from two to six GCN4 repeats. Larger oligomers caused a mitotic arrest (Fig. 5c and Extended Data Fig. 7). Thus, CENP-T$^{1–242}$'s ability to interact with spindle microtubules and impair mitotic progression increases incrementally with oligomer size.

To compare the interactions of different CENP-T$^{1–242}$ oligomer sizes, we performed quantitative immunoprecipitation–mass spectrometry on scFv–sfGFP–CENP-T$^{1–242}$ co-expressed with scaffolds with 1, 6, 10 or 18 GCN4pep repeats (1xGCN4pep, 6xGCN4pep, 10xGCN4pep and 18xGCN4pep; Extended Data Fig. 6e–g). We immunoprecipitated the tdTomato-tagged scaffolds to enrich the scaffold-bound scFv–sfGFP–CENP-T$^{1–242}$ molecules (Extended Data Fig. 6g). To compare interactions between samples, we normalized the abundances of co-immunoprecipitated proteins in each sample to the abundance of scFv–sfGFP–CENP-T$^{1–242}$ in the sample. Relative

to the immunoprecipitation of 1xGCN4pep, the NDC80 complex was enriched 1.8-fold in the 6xGCN4pep immunoprecipitation, 2.4-fold in the 10xGCN4pep immunoprecipitations and 3-fold in the 18xGCN4pep immunoprecipitation (Fig. 5d). We also observed gradual increases in the co-immunoprecipitation of MIS12 and KNL1 components, although the intermediate increases were not statistically significant (Extended Data Fig. 6h). Consistent with this gradual increase in outer kinetochore recruitment, as the number of binding sites on the scaffold increased, we observed a corresponding reduction in the levels of the NDC80 and MIS12 complexes at centromeres despite equal total cellular levels of the NDC80 complex (Fig. 5e,f and Extended Data Fig. 6i–l). Together, these results suggest that outer kinetochore recruitment by a GFP–CENP-T$^{1–242}$ molecule increases incrementally as neighbouring molecules are added. In addition, they show that an orthologous oligomerization system can recapitulate the effect of the I3-01 oligomerization system on CENP-T, which confirms that the enhancement of outer kinetochore recruitment is the result of oligomerization.

Oligomerized CENP-T uses known interactions

To confirm that this oligomerization-based outer kinetochore-recruitment activity used established assembly pathways, we introduced inhibitory mutations at the T11 and T85 phosphorylation sites, which are required for NDC80 binding (scFv–sfGFP–CENP-T$^{1–242/2A}$)[14,15,18,19,21]. scFv–sfGFP–CENP-T$^{1–242/2A}$ exhibited weaker co-localization with the NDC80 complex than wild-type scFv–sfGFP–CENP-T$^{1–242}$ when both were oligomerized with the 12xGCN4pep scaffold (Extended Data Fig. 8a,b). Furthermore, when we expressed scFv–sfGFP–CENP-T$^{1–242/2A}$ in cells, NDC80 levels at endogenous kinetochores were comparable for all scaffold sizes (Extended Data Fig. 8c,d). These results suggest that CENP-T$^{1–242}$ oligomers use CENP-T's previously defined binding sites to recruit NDC80.
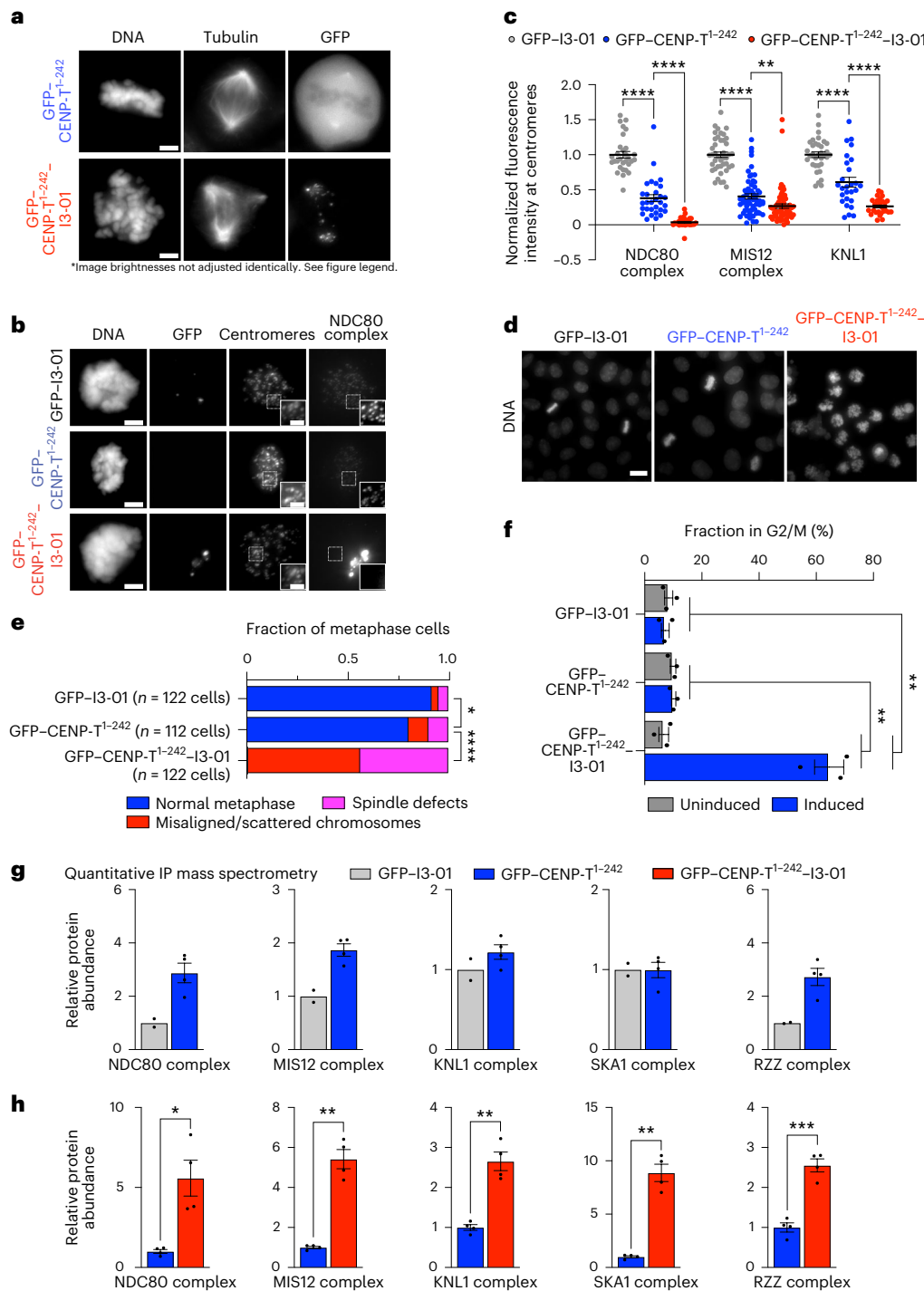
Only CENP-T oligomers saturate NDC80-binding sites

In cells, the mechanisms underlying the activation of outer kinetochore recruitment could require additional factors, such as post-translational modifications or microtubule interactions. To define the minimal requirements for enhancing CENP-T outer kinetochore recruitment by oligomerization, we reconstituted the interaction between the NDC80 complex and the CENP-T N-terminus in vitro. To activate NDC80 recruitment, we used CENP-T$^{1–242}$ constructs with the phosphomimetic substitutions T11D, T27D and T85D (GFP–CENP-T$^{1–242/3D}$) (Fig. 6a). We expressed and purified GFP–I3-01, GFP–CENP-T$^{1–242/3D}$–I3-01 and GFP–CENP-T$^{1–242/3D}$ from *Escherichia coli*, then visualized them using total internal reflection fluorescence (TIRF) microscopy. As expected, purified GFP–CENP-T$^{1–242/3D}$–I3-01 complexes appeared much brighter than the GFP–CENP-T$^{1–242/3D}$

Fig. 4 | CENP-T$^{1–242}$ oligomerization promotes outer kinetochore recruitment. **a**, Representative images of CENP-T$^{1–242}$ and GFP–CENP-T$^{1–242}$-I3-01 during mitosis. Image brightness is not scaled identically due to large differences in brightness. Repeated four times with similar results. **b**, Representative immunofluorescence of NDC80 at centromeres in mitotic cells expressing each construct. Cells are arrested in mitosis with STLC. GFP, centromere, and NDC80 channels were adjusted identically. Inset regions are indicated by dashed boxes. NDC80 insets are brighter than full-size images. Centromeres were stained with anti-centromere antibodies. Scale bar, 5 μm. Inset scale bar, 2 μm. **c**, Quantification of outer kinetochore complex signals from **b** and equivalent experiments. Bars represent mean ± s.e.m. NDC80: $n = 30$ cells for each condition pooled from two experiments. Mis12: GFP–I3-01: $n = 42$, CENP-T$^{1–242}$: $n = 57$, GFP–CENP-T$^{1–242}$–I3-01: $n = 61$ cells pooled from three experiments. KNL1: GFP–I3-01: $n = 34$, CENP-T$^{1–242}$: $n = 27$, GFP–CENP-T$^{1–242}$–I3-01: $n = 30$ cells pooled from two experiments. Two-tailed Welch's t-test: NDC80: GFP–I3-01 versus GFP–CENP-T$^{1–242}$: $P < 0.0001$; GFP–CENP-T$^{1–242}$ versus GFP–CENP-T$^{1–242}$–I3-01: $P < 0.0001$. MIS12: GFP–I3-01 versus GFP–CENP-T$^{1–242}$: $P < 0.0001$; GFP–CENP-T$^{1–242}$ versus GFP–CENP-T$^{1–242}$–I3-01: $P = 0.0047$. KNL1: GFP–I3-01 versus GFP–CENP-T$^{1–242}$: $P < 0.0001$; GFP–CENP-T$^{1–242}$ versus GFP–CENP-T$^{1–242}$–I3-01: $P < 0.0001$. **d**, Representative fields of cells

expressing each construct. Scale bar, 5 μm. Repeated four times with similar results. **e**, Distribution of mitotic errors in metaphase cells upon expression of each construct. n, number of cells in a single experiment. Repeated twice with similar results. Chi-squared test: GFP–I3-01 versus GFP–CENP-T$^{1–242}$: $P = 0.0348$; GFP–CENP-T$^{1–242}$ versus GFP–CENP-T$^{1–242}$–I3-01: $P < 0.0001$. **f**, Percentage of cells in G2/M based on DNA content measurements by flow cytometry in cell lines expressing each construct. Expression of the constructs was induced with doxycycline. Bars represent mean ± s.e.m. Each point represents a measurement from three independent experiments. Statistical analysis was performed on the differences between induced and uninduced for each condition. Two-tailed Welch's t-test: GFP–I3-01 versus GFP–CENP-T$^{1–242}$–I3-01: $P = 0.0097$; GFP–CENP-T$^{1–242}$ versus GFP–CENP-T$^{1–242}$–I3-01: $P = 0.009$. **g,h**, Comparison of outer kinetochore protein co-immunoprecipitation (IP) by GFP–I3-01 and GFP–CENP-T$^{1–242}$ (**g**) and CENP-T$^{1–242}$ CENP-T$^{1–242}$–I3-01 (**h**) as measured by quantitative mass spectrometry. Each point represents a biological replicate from one multiplexed experiment. Bars represent mean ± s.e.m. In **h**, two-tailed Welch's t-test: NDC80: $P = 0.0257$; MIS12: $P = 0.0025$; KNL1: $P = 0.0037$; SKA1: $P = 0.0021$; RZZ: $P = 0.0004$.

a

DNA | Tubulin | GFP

GFP–CENP-T$^{1-242}$

GFP–CENP-T$^{1-242}$–I3-01

*Image brightnesses not adjusted identically. See figure legend.

b

DNA | GFP | Centromeres | NDC80 complex

GFP–I3-01

GFP–CENP-T$^{1-242}$

GFP–CENP-T$^{1-242}$–I3-01

c

○ GFP–I3-01   ● GFP–CENP-T$^{1-242}$ ● GFP–CENP-T$^{1-242}$–I3-01

Normalized fluorescence intensity at centromeres

NDC80 complex | MIS12 complex | KNL1

d

GFP–I3-01 | GFP–CENP-T$^{1-242}$ | GFP–CENP-T$^{1-242}$–I3-01

DNA

e

Fraction of metaphase cells

GFP–I3-01 (*n* = 122 cells)
GFP–CENP-T$^{1-242}$ (*n* = 112 cells)
GFP–CENP-T$^{1-242}$–I3-01 (*n* = 122 cells)

■ Normal metaphase   ■ Spindle defects   ■ Misaligned/scattered chromosomes

f

Fraction in G2/M (%)

GFP–I3-01
GFP–CENP-T$^{1-242}$
GFP–CENP-T$^{1-242}$–I3-01

■ Uninduced   ■ Induced

g

Quantitative IP mass spectrometry   ■ GFP–I3-01   ■ GFP–CENP-T$^{1-242}$ ■ GFP–CENP-T$^{1-242}$–I3-01

Relative protein abundance

NDC80 complex | MIS12 complex | KNL1 complex | SKA1 complex | RZZ complex

h

Relative protein abundance

NDC80 complex | MIS12 complex | KNL1 complex | SKA1 complex | RZZ complex

monomers (Fig. 6b). By normalizing the intensity of each focus to the intensity of a single GFP fluorophore, we determined that the recombinant proteins form complexes with 44 ± 4 GFP–I3-01 molecules, 66 ± 10 GFP–CENP-T$^{1-242/3D}$ molecules, or 1.23 ± 0.05 GFP–CENP-T$^{1-242}$ molecules, consistent with the expected stoichiometries (Extended Data Fig. 9a–c).

To determine how efficiently NDC80 binds to CENP-T oligomers, we immobilized oligomers on a coverslip in a flow chamber. We determined the number of GFP–CENP-T$^{1-242/3D}$–I3-01 molecules in each oligomer by measuring its GFP signal, then we photobleached the oligomers to eliminate their GFP fluorescence. Next, we incubated them with recombinant GFP-tagged NDC80^{Bonsai} complex, a shortened version of the NDC80 complex[48] (Fig. 6c). To approximate physiological concentrations of NDC80, we used 100 nM NDC80^{Bonsai}(refs. 49,50). After a 10-min incubation, we washed away unbound NDC80^{Bonsai} and

measured the GFP signal from each focus again (Fig. 6c). By normalizing the final GFP signal of each oligomer to its initial signal, we determined the number of NDC80^{Bonsai} complexes bound to each GFP or GFP–CENP-T$^{1-242/3D}$ molecule. We found that each oligomerized molecule of GFP–CENP-T$^{1-242/3D}$ bound to 2.2 ± 0.2 NDC80^{Bonsai} molecules (Fig. 6d and Extended Data Fig. 9f). As the CENP-T N-terminus has two direct NDC80-binding sites[15,19], this result indicates that both sites in each oligomerized CENP-T molecule become saturated. GFP control oligomers did not bind to NDC80^{Bonsai} (Fig. 6d and Extended Data Fig. 9f). Furthermore, NDC80$^{\Delta Spc24/25}$ (also known as NDC80^{Broccoli}), which lacks the CENP-T-binding region of the complex[18,51], failed to interact with GFP–CENP-T$^{1-242/3D}$ oligomers (Extended Data Fig. 9d–f), confirming that the interaction depends on known CENP-T–NDC80 binding interfaces.
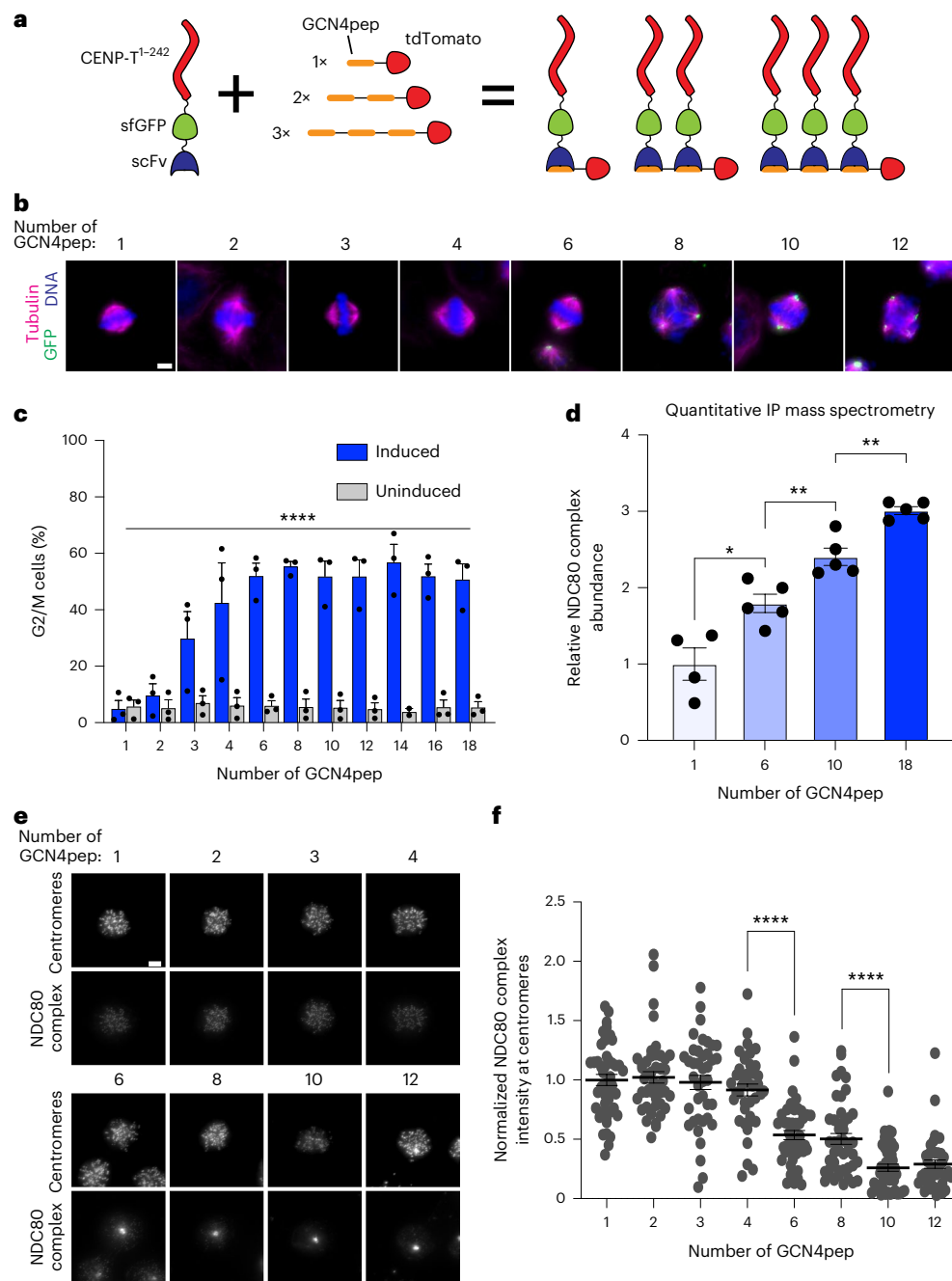
Fig. 5 | Each additional CENP-T$^{1-242}$ molecule incrementally increases outer kinetochore recruitment of neighbouring molecules. a, Diagram of SunTag oligomerization strategy. **b**, Representative immunofluorescence images of SunTag oligomer localization with different numbers of GCN4pep on the scaffold. GFP signal in all images is scaled the same. Scale bar, 5 µm. This experiment was repeated three times with similar results. **c**, Percentage of cells in G2/M based on DNA content measurements by flow cytometry in cell lines expressing SunTag with scaffolds with different numbers of GCN4pep. scFv–sfGFP–CENP-T$^{1-242}$ expression was induced with doxycycline. Bars represent mean percentage of cells in G2/M ± s.e.m. from three repeats. Welch's analysis of variance (ANOVA) test was performed on the differences between means of induced and uninduced to calculate a P value: $P < 0.0001$. **d**, Comparison of NDC80 complex co-immunoprecipitation (IP) by scaffolds with 1, 6, 10 or 18 GCN4pep copies when they were expressed alongside scFv–sfGFP–CENP-T$^{1-242}$. NDC80 complex immunoprecipitation was measured by TMT-based quantitative

mass spectrometry. TdTomato-tagged scaffolds were immunoprecipitated, then abundances were normalized and calculated as described in Methods. Each point represents a biological replicate from two multiplexed mass spectrometry runs. Each bar represents the mean ± s.e.m. Two-tailed Welch's t-test: 1 versus 6: $P = 0.0228$; 6 versus 10: $P = 0.0063$; 10 versus 18: $P = 0.0036$. **e**, Representative immunofluorescence images of NDC80 levels at centromeres in cell expressing the scFv–sfGFP–CENP-T$^{1-242}$ with scaffolds with different numbers of GCN4pep. All cells are mitotically arrested with STLC. All images use the same linear image adjustments. Scale bar, 5 µm. **f**, Quantification of NDC80 complex levels from **e**. Each point is a cell. Each bar represents the mean ± s.e.m. 1: $n = 45$; 2: $n = 45$; 3: $n = 40$; 4: $n = 40$; 6: $n = 46$; 8: $n = 45$; 10: $n = 45$; 12: $n = 40$. n, cells measured over three independent experiments. Welch's ANOVA test was performed to calculate P value for the whole dataset ($P < 0.0001$). Two-tailed Welch's t-test: 4 versus 6 and 8 versus 10: $P < 0.0001$.
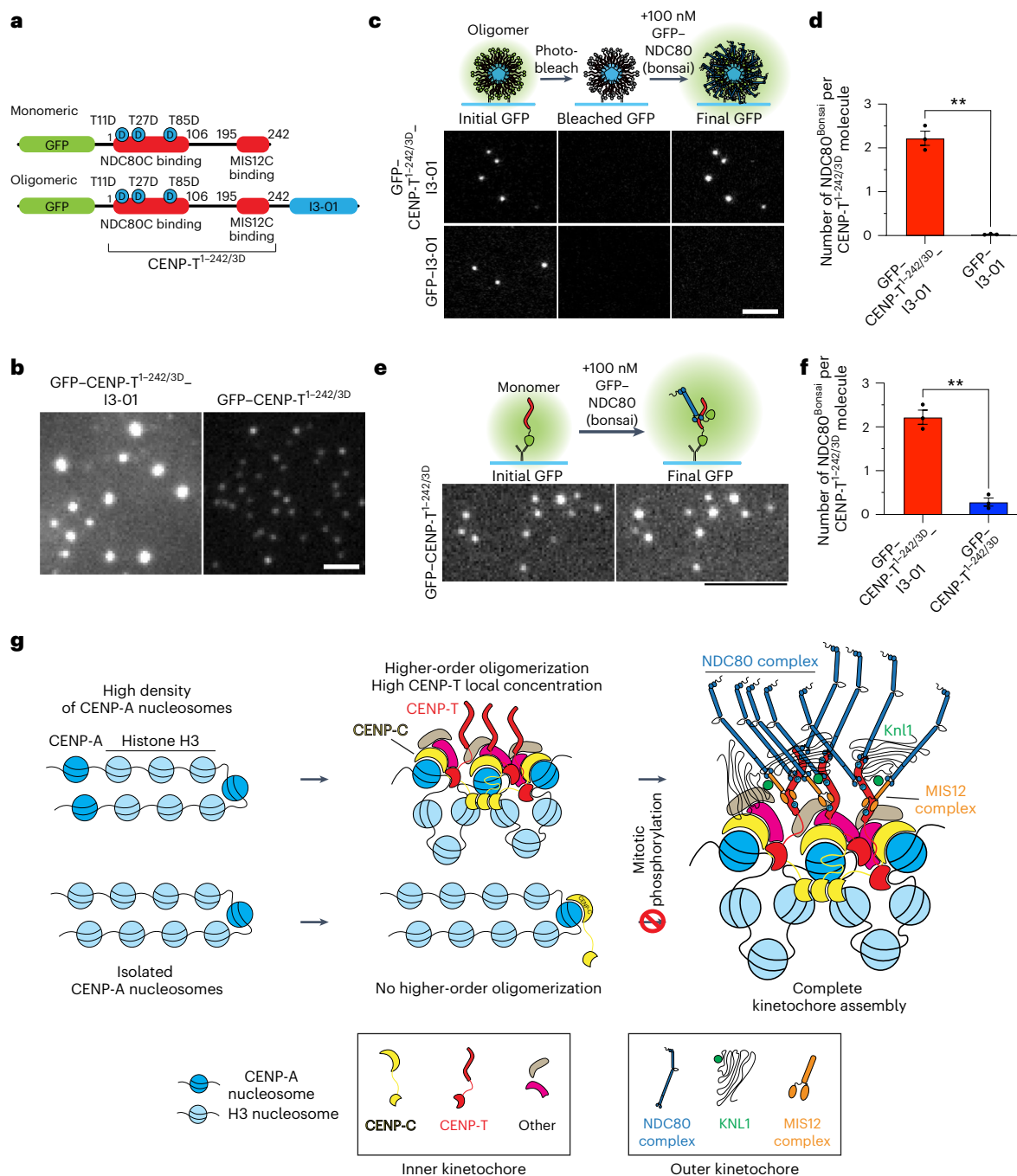
Fig. 6 | Oligomerization of CENP-T is required to saturate NDC80 binding sites. a, Diagram of recombinant constructs. Both constructs contain CENP-T$^{1-242}$ region with activating phosphomimetic substitutions at sites T11, T27 and T85. **b**, Images of GFP–CENP-T$^{1-242/3D}$–I3-01 oligomers or GFP–CENP-T$^{1-242/3D}$ monomers taken with identical microscope settings and brightness adjustments. This direct comparison was performed once. Scale bar, 2 μm. **c**, Top: diagram of single molecule experimental approach. Experimental details are described in Methods. Bottom: representative images of GFP–CENP-T$^{1-242/3TD}$–I3-01 and GFP–I3-01 oligomers at each step. Scale bar, 5 μm. **d**, Efficiency of NDC80 recruitment to GFP–CENP-T$^{1-242/3D}$–I3-01 and control GFP–I3-01 from **c**. The result is the number of NDC80 molecules bound per molecule in an oligomer. Each point is the median result from three independent trials with at least 12 oligomers. Bars are mean ± s.e.m. Two-tailed Welch's t-test: $P = 0.0051$. **e**, Top: diagram of single molecule experimental approach with GFP–CENP-T$^{1-242/3D}$ monomers. Experimental details are described in Methods. Bottom: representative examples

of GFP–CENP-T$^{1-242/3D}$ monomers before and after interaction with 100 nM GFP-tagged NDC80^{Bonsai}. Scale bar, 5 μm. **f**, Efficiency of NDC80 recruitment to GFP–CENP-T$^{1-242/3D}$–I3-01 oligomers and GFP–CENP-T$^{1-242/3TD}$ monomers from **e**. Each point is the median result from three independent trials with at least 12 oligomers or 33 monomers analysed. Bars are mean ± s.e.m. Data for GFP–CENP-T$^{1-242/3D}$–I3-01 oligomer is duplicated from **d**. Two-tailed Welch's t-test: $P = 0.0014$. **g**, Model of the role of higher-order oligomerization in kinetochore assembly. In regions where CENP-A nucleosomes are at a high density, they recruit inner kinetochore components that form higher-order assemblies. Those oligomers cluster multiple inner kinetochore modules, resulting in a high local concentration of CENP-T, which can robustly recruit the outer kinetochore during mitosis, generating complete kinetochores. When CENP-A is deposited at a low density (bottom), it may be able to recruit some inner kinetochore components, but it cannot generate a higher-order assembly. As a result, it is unable to generate the local concentration of CENP-T necessary to recruit the rest of the kinetochore.

To compare NDC80 recruitment by GFP–CENP-T$^{1–242/3D}$ oligomers to recruitment by monomers, we performed analogous experiments on monomeric GFP–CENP-T$^{1–242/3D}$ without the photobleaching step (Fig. 6e). Strikingly, each GFP–CENP-T$^{1–242/3TD}$ monomer recruited only 0.3 ± 0.1 NDC80^{Bonsai} complexes on average (Fig. 6f). Because binding events are binary, this result means that most monomeric GFP–CENP-T$^{1–242/3D}$ molecules did not bind any NDC80^{Bonsai}. In this experimental setup, only 4% of GFP molecules were photobleached, which was not sufficient to impact our results (Extended Data Fig. 9g). Thus, CENP-T$^{1–242/3D}$ must be oligomerized to saturate its direct NDC80-binding sites at physiological NDC80 concentrations in vitro. As our single molecule system lacks any other factors found in cells, these experiments also demonstrate that oligomerization dependence is an intrinsic feature of the CENP-T–NDC80 interaction independent of interactions with other factors, such as microtubules. Additionally, because both CENP-T$^{1–242}$ oligomers and monomers had identical phosphomimetic mutations, these results show that CENP-T oligomerization is a regulatory mechanism downstream of activation by mitotic phosphorylation and that the change in NDC80 binding is not mediated by changes in phosphorylation of NDC80-binding sites.

Discussion

Higher-order oligomerization directs kinetochore formation

Previous work has established a hierarchy of kinetochore recruitment to centromeres but has not explored how the higher-order organization of kinetochores contributes to their assembly. Based on prior work in vitro and in silico, the large copy numbers of proteins at individual kinetochores were thought to be necessary to form dynamic load-bearing microtubule attachments[45,52]. Here we demonstrate that this density is also a regulatory cue that may restrict kinetochore formation to centromeres.

Centromeres are specified epigenetically by histone H3-variant CENP-A[20,53]. However, the incorporation of CENP-A throughout the chromosome arms is not sufficient to trigger aberrant kinetochore formation[21,24,54,55]. By contrast, when large amounts of CENP-A are deposited at a defined genomic locus, they assemble kinetochores that can interact with mitotic spindles[56]. This difference suggests that the density of CENP-A molecules determines where the kinetochore assembles[57]. Consistent with this hypothesis, CENP-A levels at centromeres have been estimated to be 50-fold higher than CENP-A levels on the rest of the genome[58,59]. Recent work suggests that the CENP-A-binding proteins CENP-C and CENP-N may generate higher-order assemblies of CENP-A-associated inner kinetochore complexes[5,6]. Evidence from other higher-order assemblies indicates that formation of these structures is often controlled by regulated nucleation steps[10]. Dense deposition of CENP-A may fulfil that role in the formation of higher-order kinetochore assemblies by increasing the effective concentration of CENP-A-associated inner kinetochore proteins, triggering oligomerization. Our work reveals a mechanism by which formation of these higher-order assemblies can regulate the formation of functional kinetochores by restricting outer kinetochore recruitment to regions with a high density of inner kinetochore complexes. When dense deposition of CENP-A at centromeres nucleates oligomerization of inner kinetochore modules, the CENP-T molecules in those modules are clustered, which primes the inner kinetochore for outer kinetochore recruitment during mitosis (Fig. 6g). Although CENP-T does not independently form oligomers, the oligomerization activity of other inner kinetochore proteins brings together CENP-T molecules from multiple inner kinetochore modules. This paradigm for controlling kinetochore formation is complementary to previously defined regulation, such as post-translational modifications. Our in vitro experiments with phosphomimetic CENP-T mutants suggest that, even when kinase activity is permissive, the dependence on higher-order assembly prevents aberrant formation of functional outer kinetochore

complexes at non-centromeric sites on chromosomes and on cytoplasmic kinetochore components that have not been incorporated into chromatin[29].

Biophysical analysis of kinetochore-like particles

In vitro biophysical analysis of kinetochores depends on tools that can recapitulate endogenous kinetochore–microtubule interactions outside of cells. In budding yeast, which have much smaller point centromeres, it is possible to isolate intact kinetochore complexes for in vitro analysis[59–62]. However, biophysical studies of the more complex vertebrate kinetochore have been limited to simplified systems such as the NDC80 complex alone or assemblies of the NDC80 and SKA1 complexes[51,61,63–67]. CENP-T-based ectopic kinetochores formed on chromosomal *lacO* arrays are functional and rescue excision of endogenous kinetochores[21,68]. Here we used a related strategy to generate soluble kinetochore-like particles that can be isolated from cells. These CENP-T particles are compositionally and mechanically similar to endogenous human kinetochores and are sufficiently tractable for in vitro applications, enabling future biophysical investigation of the mechanical properties of complete human kinetochores.

Concentration-dependent regulation of protein activity

Recent interest in higher-order protein assemblies has focused on liquid–liquid phase separation as a mechanism for locally concentrating interacting partners[11]. These membrane-less compartments are thought to form through the interactions of proteins with disordered regions that contain multivalent low-affinity interfaces with dissociation constants in the micromolar or millimolar ranges[10,69,70]. Like those proteins, human CENP-T is multivalent and disordered[2,15,19]. However, unlike putative phase-separating scaffolds, CENP-T uses high affinity binding sites with nanomolar dissociation constants to interact with outer kinetochore proteins[16,18,25], and CENP-T is recruited to the inner kinetochore by site-specific interactions[34]. Furthermore, the transition from a homogenous mixture to a phase separated solution is binary and happens when a phase-separating scaffold achieves its saturation concentration[11], which is not consistent with the gradual change in binding that we observed with the SunTag system. As a result, existing models of phase separation are unlikely to explain our findings. Although low-affinity interactions may also play a role, our work suggests that high local concentrations modulate CENP-T activity in a manner that remains dependent on specific high-affinity interactions to enable stable binding.

Like kinetochores, other biological pathways are thought to use higher-order assemblies to regulate their activities. For example, numerous signal transduction pathways form massive complexes called 'signalosomes' to initiate intracellular signalling[10,71–74]. Establishing direct links between oligomerization and function for these higher-order assemblies has been challenging. The toolkit used here could prove valuable for investigating these relationships. Unlike popular higher-order oligomerization systems such as the optogenetic CRY2 system, the I3-01 and SunTag oligomerization systems generate stable and tunable oligomers, respectively[35,47,75,76]. These oligomers can be purified for in vitro applications and used to study the stoichiometries that govern the activities of higher-order assemblies. Our approach is readily applicable to other proteins that have distinct oligomerization and functional domains, both at the kinetochore and in unrelated pathways.

Online content

Any methods, additional references, Nature Portfolio reporting summaries, source data, extended data, supplementary information, acknowledgements, peer review information; details of author contributions and competing interests; and statements of data and code availability are available at https://doi.org/10.1038/s41556-023-01313-7.

References

1. Cheeseman, I. M. The kinetochore. *Cold Spring Harb. Perspect. Biol.* https://doi.org/10.1101/cshperspect.a015826 (2014).
2. Musacchio, A. & Desai, A. A molecular view of kinetochore assembly and function. *Biology* **6**, 5 (2017).
3. Suzuki, A., Badger, B. L. & Salmon, E. D. A quantitative description of Ndc80 complex linkage to human kinetochores. *Nat. Commun.* https://doi.org/10.1038/ncomms9161 (2015).
4. Brinkley, B. R. & Cart Wright, J. Ultrastructural analysis of mitotic spindle elongation in mammalian cells in vitro. Direct microtubule counts. *J. Cell Biol.* **50**, 416–431 (1971).
5. Zhou, K. et al. CENP-N promotes the compaction of centromeric chromatin. *Nat. Struct. Mol. Biol.* **29**, 403–413 (2022).
6. Hara, M. et al. Centromere/kinetochore is assembled through CENP-C oligomerization. *Mol. Cell* https://doi.org/10.1016/j.molcel.2023.05.023 (2023).
7. Cheeseman, I. M. & Desai, A. Molecular architecture of the kinetochore–microtubule interface. *Nat. Rev. Mol. Cell Biol.* **9**, 33–46 (2008).
8. Xia, S. et al. Higher-order assemblies in immune signaling: supramolecular complexes and phase separation. *Protein Cell* **12**, 680 (2021).
9. Wu, H. Higher-order assemblies in a new paradigm of signal transduction. *Cell* **153**, 287–292 (2013).
10. Wu, H. & Fuxreiter, M. The structure and dynamics of higher-order assemblies: amyloids, signalosomes, and granules. *Cell* **165**, 1055–1066 (2016).
11. Banani, S. F. et al. Biomolecular condensates: organizers of cellular biochemistry. *Nat. Rev. Mol. Cell Biol.* **18**, 285–298 (2017).
12. Marzahn, M. R. et al. Higher-order oligomerization promotes localization of SPOP to liquid nuclear speckles. *EMBO J.* **35**, 1254–1275 (2016).
13. Navarro, A. P. & Cheeseman, I. M. Kinetochore assembly throughout the cell cycle. *Semin. Cell Dev. Biol.* **117**, 62–74 (2021).
14. Gascoigne, K. E. & Cheeseman, I. M. CDK-dependent phosphorylation and nuclear exclusion coordinately control kinetochore assembly state. *J. Cell Biol.* **201**, 23–32 (2013).
15. Rago, F., Gascoigne, K. E. & Cheeseman, I. M. Distinct organization and regulation of the outer kinetochore KMN network downstream of CENP-C and CENP-T. *Curr. Biol.* **25**, 671–677 (2015).
16. Hara, M. et al. Multiple phosphorylations control recruitment of the KMN network onto kinetochores. *Nat. Cell Biol.* **20**, 1378–1388 (2018).
17. Kim, S. & Yu, H. Multiple assembly mechanisms anchor the KMN spindle checkpoint platform at human mitotic kinetochores. *J. Cell Biol.* **208**, 181–196 (2015).
18. Nishino, T. et al. CENP-T provides a structural platform for outer kinetochore assembly. *EMBO J.* **32**, 424–436 (2013).
19. Huis In 't Veld, P. J. et al. Molecular basis of outer kinetochore assembly on CENP-T. *eLife* https://doi.org/10.7554/eLife.21007 (2016).
20. Palladino, J. et al. Targeted *de novo* centromere formation in *Drosophila* reveals plasticity and maintenance potential of CENP-A chromatin. *Dev. Cell* **52**, 379–394.e7 (2020).
21. Gascoigne, K. E. et al. Induced ectopic kinetochore assembly bypasses the requirement for CENP-A nucleosomes. *Cell* https://doi.org/10.1016/j.cell.2011.03.031 (2011).
22. Gascoigne, K. E. & Cheeseman, I. M. Induced dicentric chromosome formation promotes genomic rearrangements and tumorigenesis. *Chromosome Res.* **21**, 407–418 (2013).
23. Mckinley, K. L. & Cheeseman, I. M. The molecular basis for centromere identity and function. *Nat. Publ. Group* **17**, 16–29 (2015).
24. Van Hooser, A. A. et al. Specification of kinetochore-forming chromatin by the histone H3 variant CENP-A. *J. Cell Sci.* **114**, 3529–3542 (2001).
25. Walstein, K. et al. Assembly principles and stoichiometry of a complete human kinetochore module. *Sci. Adv.* **7**, 27 (2021).
26. Yatskevich, S. et al. Structure of the human inner kinetochore bound to a centromeric CENP-A nucleosome. *Science* **376**, 844–852 (2022).
27. Pesenti, M. E. et al. Structure of the human inner kinetochore CCAN complex and its significance for human centromere organization. *Mol. Cell* **82**, 2113–2131.e8 (2022).
28. Tian, T. et al. Structural insights into human CCAN complex assembled onto DNA. *Cell Discov.* **8**, 1–15 (2022).
29. Tarasovetc, E. V. et al. Permitted and restricted steps of human kinetochore assembly in mitotic cell extracts. *Mol. Biol. Cell* **32**, 1241–1255 (2021).
30. Screpanti, E. et al. Direct binding of Cenp-C to the Mis12 complex joins the inner and outer kinetochore. *Curr. Biol.* **21**, 391–398 (2011).
31. Petrovic, A. et al. The MIS12 complex is a protein interaction hub for outer kinetochore assembly. *J. Cell Biol.* **190**, 835–852 (2010).
32. Drinnenberg, I. A., Henikoff, S. & Malik, H. S. Evolutionary turnover of kinetochore proteins: a ship of Theseus? *Trends Cell Biol.* **26**, 498–510 (2016).
33. Takenoshita, Y., Hara, M. & Fukagawa, T. Recruitment of two Ndc80 complexes via the CENP-T pathway is sufficient for kinetochore functions. *Nat. Commun.* **13**, 1–19 (2022).
34. Nishino, T. et al. CENP-T-W-S-X forms a unique centromeric chromatin structure with a histone-like fold. *Cell* **148**, 487–501 (2012).
35. Hsia, Y. et al. Design of a hyperstable 60-subunit protein icosahedron. *Nature* **535**, 136–139 (2016).
36. Hori, T. et al. CCAN makes multiple contacts with centromeric DNA to provide distinct pathways to the outer kinetochore. *Cell* **135**, 1039–1052 (2008).
37. Musacchio, A. The molecular biology of spindle assembly checkpoint signaling dynamics. *Curr. Biol.* **25**, R1002–R1018 (2015).
38. Monda, J. K. & Cheeseman, I. M. The kinetochore–microtubule interface at a glance. *J. Cell Sci.* **131**, jcs214577 (2018).
39. Kops, G. J. P. L. & Gassmann, R. Crowning the kinetochore: the fibrous corona in chromosome segregation. *Trends Cell Biol.* **30**, 653–667 (2020).
40. Grishchuk, E. L. Biophysics of microtubule end coupling at the kinetochore. *Prog. Mol. Subcell. Biol.* **56**, 397–428 (2017).
41. Maiato, H. et al. Mechanisms of chromosome congression during mitosis. *Biology* **6**, 13 (2017).
42. Cheeseman, I. M. et al. The conserved KMN network constitutes the core microtubule-binding site of the kinetochore. *Cell* **127**, 983–997 (2006).
43. Cai, S. et al. Chromosome congression in the absence of kinetochore fibres. *Nat. Cell Biol.* **11**, 832–838 (2009).
44. Hunt, A. J. & McIntosh, J. R. The dynamic behavior of individual microtubules associated with chromosomes in vitro. *Mol. Biol. Cell* **9**, 2857–2871 (1998).
45. Volkov, V. A. et al. Multivalency of NDC80 in the outer kinetochore is essential to track shortening microtubules and generate forces. *eLife* **7**, e36764 (2018).
46. Zaytsev, A. V., Ataullakhanov, F. I. & Grishchuk, E. L. Highly transient molecular interactions underlie the stability of kinetochore–microtubule attachment during cell division. *Cell. Mol. Bioeng.* **6**, 393–405 (2013).
47. Tanenbaum, M. E. et al. A protein-tagging system for signal amplification in gene expression and fluorescence imaging. *Cell* **159**, 635–646 (2014).

48. Ciferri, C. et al. Implications for kinetochore–microtubule attachment from the structure of an engineered Ndc80 complex. *Cell* **133**, 427–439 (2008).

49. Itzhak, D. N. et al. Global, quantitative and dynamic mapping of protein subcellular localization. *eLife* **5**, e16950 (2016).

50. Wiśniewski, J. R. et al. A "proteomic ruler" for protein copy number and concentration estimation without spike-in standards. *Mol. Cell. Proteom.* **13**, 3497–3506 (2014).

51. Schmidt, J. C. et al. The kinetochore-bound Ska1 complex tracks depolymerizing microtubules and binds to curved protofilaments. *Dev. Cell* **23**, 968–980 (2012).

52. Zaytsev, A. V. et al. Accurate phosphoregulation of kinetochore–microtubule affinity requires unconstrained molecular interactions. *J. Cell Biol.* **206**, 45–59 (2014).

53. McKinley, K. L. & Cheeseman, I. M. The molecular basis for centromere identity and function. *Nat. Rev. Mol. Cell Biol.* **17**, 16–29 (2015).

54. Nechemia-Arbely, Y. et al. DNA replication acts as an error correction mechanism to maintain centromere identity by restricting CENP-A to centromeres. *Nat. Cell Biol.* **21**, 743 (2019).

55. Athwal, R. K. et al. CENP-A nucleosomes localize to transcription factor hotspots and subtelomeric sites in human cancer cells. *Epigenet. Chromatin* **8**, 23 (2015).

56. Barnhart, M. C. et al. HJURP is a CENP-A chromatin assembly factor sufficient to form a functional de novo kinetochore. *J. Cell Biol.* **194**, 229–243 (2011).

57. De Rop, V., Padeganeh, A. & Maddox, P. S. CENP-A: the key player behind centromere identity, propagation, and kinetochore assembly. *Chromosoma* **121**, 527 (2012).

58. Bodor, D. L. et al. The quantitative architecture of centromeric chromatin. *eLife* **3**, e02137 (2014).

59. Akiyoshi, B. et al. Quantitative proteomic analysis of purified yeast kinetochores identifies a PP1 regulatory subunit. *Genes Dev.* **23**, 2887–2899 (2009).

60. Akiyoshi, B. et al. Tension directly stabilizes reconstituted kinetochore–microtubule attachments. *Nature* **468**, 576–579 (2010).

61. Miller, M. P., Asbury, C. L. & Biggins, S. A TOG protein confers tension sensitivity to kinetochore–microtubule attachments. *Cell* **165**, 1428–1439 (2016).

62. Gonen, S. et al. The structure of purified kinetochores reveals multiple microtubule-attachment sites. *Nat. Struct. Mol. Biol.* **19**, 925–929 (2012).

63. Powers, A. F. et al. The Ndc80 kinetochore complex forms load-bearing attachments to dynamic microtubule tips via biased diffusion. *Cell* **136**, 865–875 (2009).

64. Helgeson, L. A. et al. Human Ska complex and Ndc80 complex interact to form a load-bearing assembly that strengthens kinetochore–microtubule attachments. *Proc. Natl Acad. Sci. USA* **115**, 2740–2745 (2018).

65. Huis in'T Veld, P. J. et al. Molecular determinants of the Ska–Ndc80 interaction and their influence on microtubule tracking and force-coupling. *eLife* **8**, e49539 (2019).

66. Luo, W. et al. CLASP2 recognizes tubulins exposed at the microtubule plus-end in a nucleotide state-sensitive manner. *Sci. Adv.* **9**, eabq5404 (2023).

67. Chakraborty, M. et al. Microtubule end conversion mediated by motors and diffusing proteins with no intrinsic microtubule end-binding activity. *Nat. Commun.* **10**, 1–14 (2019).

68. Hori, T. et al. The CCAN recruits CENP-A to the centromere and forms the structural core for kinetochore assembly. *J. Cell Biol.* **200**, 45–60 (2013).

69. Bhat, P., Honson, D. & Guttman, M. Nuclear compartmentalization as a mechanism of quantitative control of gene expression. *Nat. Rev. Mol. Cell Biol.* **22**, 653–670 (2021).

70. Li, P. et al. Phase transitions in the assembly of multivalent signalling proteins. *Nature* **483**, 336–340 (2012).

71. Schwarz-Romond, T. et al. The DIX domain of Dishevelled confers Wnt signaling by dynamic polymerization. *Nat. Struct. Mol. Biol.* **14**, 484–492 (2007).

72. Li, J. et al. The RIP1/RIP3 necrosome forms a functional amyloid signaling complex required for programmed necrosis. *Cell* **150**, 339–350 (2012).

73. Lu, A. et al. Plasticity in PYD assembly revealed by cryo-EM structure of the PYD filament of AIM2. *Cell Discov.* **1**, 1–14 (2015).

74. Lu, A. & Wu, H. Structural mechanisms of inflammasome assembly. *FEBS J.* **282**, 435–444 (2015).

75. Park, H. et al. Optogenetic protein clustering through fluorescent protein tagging and extension of CRY2. *Nat. Commun.* **8**, 1–8 (2017).

76. Bugaj, L. J. et al. Optogenetic protein clustering and signaling activation in mammalian cells. *Nat. Methods* **10**, 249–252 (2013).

Methods

Plasmid cloning

The *I3-01* gene was synthesized by Genewiz. *sfGFP–scFv* tag and *CENP-T[1–242/2A]* were synthesized by Twist Bioscience. SunTag scaffolds were obtained from pcDNA4TO-mito–mCherry–24xGCN4_v1, which was a gift from Ron Vale (Addgene plasmid #60913). CENP-T[1–242] was obtained from pKG174[21]. Lentiviral plasmids were generated from Lenti-Cas9-2A-Blast, which was a gift from Jason Moffat (Addgene plasmid #73310). Plasmids have been deposited to Addgene.

Cell line generation

The cell lines used in this study are described in Supplementary Table 1. All cell lines are in a HeLa cell background using Cheeseman lab HeLa cells. Doxycycline-inducible cell lines were generated by homology-directed insertion into the AAVS1 'safe-harbour' locus. Donor plasmid containing selection marker, the tetracycline-responsive promoter, the transgene, and reverse tetracycline-controlled trans-activator flanked by AAVS1 homology arms[77] was transfected using Lipofectamine 2000 with a pX330-based plasmid[78] expressing both spCas9 and a guide RNA specific for the AAVS1 locus (pNM220; gRNA sequence 5'-GGGGCCACTAGGGACAGGAT). Cells were selected with 0.5 μg ml^{−1} puromycin (Life Technologies). Clonal lines were obtained by fluorescence-activated cell-sorting single cells into 96-well plates.

Cell lines containing SunTag scaffolds were generated by lentiviral transduction. Lentivirus was generated by using Xtremegene-9 (Roche 06365787001) to co-transfect the scaffold-containing pLenti plasmid, VSV-G envelope plasmid, and Delta-VPR or psPAX2 (gift from Didier Trono; Addgene plasmid #12260) packaging plasmids into HEK-293T cells[79]. Lentivirus cell lines were selected with 2 μg ml^{−1} blasticidin (Life Technologies). Cell lines containing SunTag scaffolds were generated from clonal parental lines expressing the desired sfGFP–scFv construct at comparable levels.

Expression of constructs was validated by western blot for each cell line (CGS50, cGS49, cGS50 and cGS54: Extended Data Fig. 4d; cGS365–374 and cGS386: Extended Data Fig. 6b,d; cGS257, cGS261, cGS263 and cGS267: Extended Data Fig. 6e,f; cGS416–423: Extended Data Fig. 6j,l; cGS642–649: Extended Data Fig. 8d).

Cell culture

HeLa cells were cultured in Dulbecco's modified Eagle medium supplemented with 10% foetal bovine serum, 100 U ml^{−1} penicillin and streptomycin, and 2 mM L-glutamine at 37 °C with 5% CO₂. TetOn cell lines were cultured in foetal bovine serum certified as tetracycline-free. TetOn constructs were induced with 1 μg ml^{−1} doxycycline for 24 h. To depolymerize microtubules, cells were treated with 3.3 μM nocodazole for 16 h. To arrest cells in mitosis, cells were treated with 10 μM *S*-trityl-L-cysteine (STLC) for 16 h. HeLa cells were regularly monitored for mycoplasma contamination.

Western blot

Cells were collected by trypsinization and resuspended, then washed with phosphate-buffered saline (PBS) and immediately lysed on ice for 30 min in fresh urea lysis buffer (50 mM Tris pH 7.5, 150 mM NaCl, 0.5% NP-40, 0.1% sodium dodecyl sulfate (SDS), 6.5 M urea, 1× complete ethylenediaminetetraacetic acid (EDTA)-free protease inhibitor cocktail (Roche) and 1 mM phenylmethylsulfonyl fluoride (PMSF)) or cells lysed directly on plate with RIPA buffer (150 mM NaCl, 1% Nonident P-40 substitute, 0.5% sodium deoxycholate, 0.1% SDS, 50 mM Tris pH 7.5, 1× complete EDTA-free protease inhibitor cocktail (Roche) and 1 mM PMSF) on ice. Protein concentrations were measured using either Bradford reagent (Bio-Rad) or BCA protein assay kit (Pierce) and used to normalize loading. Antibodies and antibody sources are listed in Supplementary Table 2[21,51,80–83]. Primary antibodies were diluted in Blocking Buffer and applied to the membrane for 1 h. Horseradish peroxidase-conjugated secondary antibodies (GE Healthcare; Digital) were diluted in Tris-buffered saline with 0.1% Tween-20 (TBST). Clarity enhanced chemiluminescence substrate (Bio-Rad) was used according to the manufacturer's instructions. All blots were imaged with a KwikQuant Imager (Kindle Biosciences) except for the long-exposure image in Extended Data Fig. 6e, which was imaged with ChemiDoc Imaging System (Bio-Rad). Horseradish peroxidase was quenched by agitation in 0.2% sodium azide in TBST for at least 1 h.

Immunofluorescence and microscopy of mitotic cells

Cells were seeded on poly-L-lysine (Sigma-Aldrich) coated coverslips and fixed as indicated in Supplementary Table 3. Coverslips were washed with 0.1% PBS-Tx (PBS with 0.1% Triton X-100) and blocked in Abdil (20 mM Tris–HCl, 150 mM NaCl, 0.1% Triton X-100, 3% bovine serum albumin (BSA) and 0.1% NaN₃, pH 7.5). Primary antibodies used in this study are described in Supplementary Table 2 and were diluted in Abdil. Dilutions are listed in Supplementary Table 2. Cy3- and Cy5-conjugated (or Alexa647-conjugated) secondary antibodies (Jackson ImmunoResearch Laboratories) were diluted 1:300 in 0.1% PBS-Tx. DNA was stained with 1 μg ml^{−1} Hoechst-33342 (Sigma-Aldrich) in 0.1% PBS-Tx for 10 min. Coverslips were mounted with PPDM (0.5% *p*-phenylenediamine, 20 mM Tris–HCl, pH 8.8, and 90% glycerol). Images were acquired with a DeltaVision Ultra High-Resolution microscope (Imsol) and deconvolved where indicated. All images are maximal intensity projections in *z*. Image analysis and manipulation was performed in Fiji (ImageJ, NIH)[84].

Integrated fluorescence intensity of mitotic centromeres was measured with a custom CellProfiler 4.0 pipeline[85] (adapted from McQuin et al. 2014). The median intensity of a 5-pixel region surrounding each centromere was multiplied by the area of the centromere to determine background intensity. Regions with high GFP signal were masked to avoid measuring kinetochore proteins bound to GFP-tagged constructs. Values for each cell were calculated from the mean of the outer kinetochore protein antibody signals of kinetochores in that cell. Before calculating the mean for a cell, the kinetochore protein antibody intensity of each kinetochore in the cell was normalized to anti-centromere antibody signal from that kinetochore. Overall means were calculated from pooled data from multiple experiments. To make results comparable between experiments, the mean for each cell was normalized to the mean of all cells in the GFP–I3-01 control sample in the same experiment. All image quantifications were performed on raw pixel values.

Quantifications of co-localization were performed on *Z*-stacks using a custom cell Profiler 4.0 pipeline[85]. Because many kinetochore antibodies have non-specific localization to spindles and kinetochores interact with mitotic spindles, which is a confounding factor when measuring co-localization with constructs that also interact with spindles, co-localization quantifications in Fig. 2b and Extended Data Fig. 1b were performed on cells treated with 3.3 μM nocodazole to completely depolymerize spindles. For co-localization analyses of cells fixed with PHEM (PIPES, HEPES, EGTA, magnesium sulfate heptahydrate) Pre-extraction (Supplementary Table 3), α-tubulin channel was used to identify cells. For co-localization analyses of cells fixed with PBS Pre-extraction (Supplementary Table 3), DNA channel was used to identify cells.

DNA content analysis

Cells were incubated in 1 μg ml^{−1} doxycycline for 24 h. Then 5 mM EDTA, 20 μg ml^{−1} Hoechst-33342 (Sigma-Aldrich) and 10 μM Verapimil (Tocris; Spirochrome) were added directly to media for 30 min to 1 h to detach cells from the plate and stain them. Cells were collected and filtered through 35-μm nylon mesh (Falcon). Hoechst, GFP and tdTomato signals were measured on an LSRFortessa (BD Biosciences) flow cytometer. Results were analysed with FlowJo software. Example gating strategy for SunTag system is shown in Extended Data Fig. 7. The fraction of cells in each cell cycle phase was determined in FlowJo with

a Watson (Pragmatic) model using the Cell Cycle tool. The DNA content of at least 9,000 cells was analysed for each condition per experiment.

Crosslinking immunoprecipitation–mass spectrometry

Construct expression was induced, and cells were arrested in mitosis as described in the 'Cell culture' section. They were collected 24 h after doxycycline addition and 16 h after STLC addition by mitotic shake-off. Mitotic cells were centrifuged at 250g and resuspended in Crosslinking Buffer (20 mM HEPES pH 7.5, 10 mM KCl, 1.5 mM MgCl$_2$ and 1 mM dithiothreitol (DTT)). To crosslink samples, formaldehyde was added to 0.1% and samples were incubated at 37 °C for 15 min. Glycine was added to 0.25 M to quench formaldehyde. Samples were washed once in PBS and once in lysis buffer without detergent (25 mM HEPES pH 8.0, 2 mM MgCl$_2$, 0.1 mM EDTA pH 8.0, 0.5 mM egtazic acid (EGTA) pH 8.0, 150 mM KCl and 15% glycerol).

To prepare protein extracts, samples were thawed and an equal volume of 1.5× high-salt lysis buffer with detergent (37.5 mM HEPES pH 8.0, 3 mM MgCl$_2$, 0.15 mM EDTA pH 8.0, 0.75 mM EGTA pH 8.0, 450 mM KCl, 15% glycerol and 0.225% Nonidet P-40 substitute) was added. Proteases were inhibited with a tablet of complete EDTA-free protease inhibitor cocktail (Roche) and 1 mM PMSF. Phosphatases were inhibited with 0.4 mM sodium orthovanadate, 5 mM sodium fluoride and 20 mM β-glycerophosphate. Cells were lysed with Branson Digital Sonifier tip sonicator to shear DNA. Lysates were for incubated 1 h at room temperature with Protein A beads (Bio-Rad) coupled to anti-GFP or anti-mCherry antibodies (Cheeseman lab; mCherry antibodies validated in Extended Data Fig. 6g). After incubation, beads were washed in lysis buffer with high salt, DTT and LPC (25 mM HEPES pH 8.0, 2 mM MgCl$_2$, 0.1 mM EDTA pH 8.0, 0.5 mM EGTA pH 8.0, 300 mM KCl, 15% glycerol, 0.15% Nonidet P-40 substitute, 1 mM DTT, 10 µg ml^{-1} leupeptin (Millipore), 10 µg ml^{-1} pepstatin (Thermo Fisher Scientific) and 10 µg ml^{-1} chymostatin (Millipore)), then washed in the same buffer without detergent once (25 mM HEPES pH 8.0, 2 mM MgCl$_2$, 0.1 mM EDTA pH 8.0, 0.5 mM EGTA pH 8.0, 300 mM KCl, 15% glycerol, 1 mM DTT, 10 µg ml^{-1} leupeptin (Millipore), 10 µg ml^{-1} pepstatin (Thermo Fisher Scientific) and 10 µg ml^{-1} chymostatin (Millipore)). Beads were incubated in 0.1 M glycine pH 2.6 for 5 min three times and once with lysis buffer without detergent to elute. Elutions were pooled, and Tris pH 8.5 was added to 200 mM. Eluate was incubated at 65 °C for 1.5 h to reverse crosslinks. Proteins were precipitated with 20% trichloroacetic acid (Fisher Bioreagents) overnight on ice. The next day, samples were centrifuged at 20,817g at 4 °C. Pellets were washed twice with ice-cold acetone. Samples were dried in Eppendorf Vacufuge and stored at −80 °C.

Samples were resuspended in SDS lysis buffer (5%, 50 mM tetraethylammonium bromide pH 8.5), then DTT was added to 20 mM and samples were incubated at 95 °C for 10 min. After cooling to room temperature, samples were treated 40 mM iodoacetamide (Sigma) for 30 min in the dark. Samples were acidified with 1.2% phosphoric acid, then run over S-Trap microcolumns (ProtiFi), digested on the columns, and eluted as described in ProtiFi S-trap micro kit protocol. We quantified eluate peptide concentration with Quantitative Fluorometric Peptide Assay (Pierce). We lyophilized remaining eluate to remove solvent and stored at −80 °C.

For quantitative mass spectrometry, up to 19 samples were prepared simultaneously as described above. Each sample was incubated with a different TMT10plex label (Thermo Fisher Scientific) in 30% acetonitrile, 24.5 mM tetraethylammonium bromide pH 8.5 for 1 h at room temperature. TMT10plex reagents were added to labelling reactions in a ten-fold excess over peptides by mass. The labelling reaction was quenched by adding hydroxylamine to 0.3% and incubating for 15 min at room temperature. Labelled samples were pooled, then lyophilized to remove solvent and stored at −80 °C.

To removed salt and labels and to increase coverage, samples were fractionated with High pH Reversed-Phase Peptide Fractionation

kit (Pierce). After fractionation, fractions were lyophilized and resuspended in 0.1% formic acid. Samples were analysed on an Orbitrap Exploris 480 connected to an EASY-nLC chromatography system using two compensation voltages applied with a FAIMS Pro Interface (Thermo Fisher Scientific). Proteins were identified in Proteome Discoverer 2.4 (Thermo Fisher Scientific) using Sequest HT. Peptide-spectrum matches were validated using Percolator.

Tandem mass tag quantification was done in Proteome Discoverer. For quantitative mass spectrometry, We normalized all outer kinetochore protein peptide abundances to the sum of the abundances of peptides shared between pairs of bait proteins. For example, in comparisons between GFP–CENP-T$^{1–242}$–I3-01 and GFP–CENP-T$^{1–242}$, we calculated the sum of the abundances of all GFP–CENP-T$^{1–242}$ peptides, which are found in both constructs. For each biological replicate, peptide abundances from outer kinetochore proteins were normalized to the sum of abundances of GFP–CENP-T$^{1–242}$ peptides in the same biological replicate. The abundance of a given protein or complex was obtained from the sum of normalized abundances of all peptides within that protein or complex. For SunTag experiments with more than ten total samples (Fig. 5d), the results from multiple TMT10plex runs were combined. A technical replicate of one of the samples was included in each of the two runs for batch normalization. Only peptides with quantification data for all samples in both runs were included in the analysis. For each replicate in both runs, the abundance of each peptide was normalized to the total abundance of peptides from sfGFP–scFv–CENP-T$^{1–242}$. After that normalization step, the abundance of each peptide for all samples in each run was normalized to the abundance of the same peptide in the technical replicate that was included in both runs for batch normalization. The resulting values were used for the final analysis.

Isolation of CENP-T-based kinetochore-like particles from HeLa cells

HeLa cells with doxycycline inducible expression of GFP–I3-01 or GFP–CENP-T$^{1–242}$–I3-01 were cultured in 15-cm tissue culture plates. After cells reached 70–90% confluence, expression of oligomers was induced by addition of 1 µg ml^{-1} doxycycline (Sigma-Aldrich, D9891) for 24 h. Mitotic cells were collected by shaking off and gently rinsing with a pipette. Collected cells were pelleted by centrifugation at 1,000g and washed in DPBS buffer (Corning, 21-031-CV). Cells were resuspended in lysis buffer (50 mM HEPES pH 7.2, 2 mM MgCl$_2$, 150 mM K-glutamate, 0.1 mM EDTA, 2 mM EGTA and 10% glycerol) and pelleted by centrifugation. Cell pellets containing ~10^7 cells were snap-frozen and stored in liquid nitrogen. Pellets of cells expressing GFP–I3-01 oligomers were prepared analogously except the mitotic cells were induced by adding 10 µM STLC (Sigma-Aldrich, 164739) for 14 h.

GFP–CENP-T$^{1–242}$–I3-01 and GFP–I3-01 oligomers were isolated from mitotic cell extracts prepared as in Tarasovetc et al. 2021 (ref. 29). Briefly, one frozen cell pellet (~100 µl) was resuspended in two volumes of ice-cold lysis buffer supplemented with 0.1% IGEPAL (Sigma-Aldrich, I8896), 4 mM Mg-ATP, 2 mM DTT, protease inhibitors (0.2 mM 4-(2-aminoethyl)-benzenesulfonylfluoride hydrochloride (Goldbiom, A-540-5), 10 µg ml^{-1} leupeptin (Roche, 11017128001), 10 µg ml^{-1} pepstatin (Roche, 11359053001), 10 µg ml^{-1} chymostatin (Sigma-Aldrich, C7268), Complete Mini EDTA-free cocktail (Roche, 11836170001)), phosphatase inhibitors (100 ng ml^{-1} microcystin-LR (Enzo Life Sciences, ALX-350-012), 1 mM sodium pyrophosphate (Sigma-Aldrich, P8010), 2 mM sodium-beta-glycerophosphate (Santa Cruz Biotechnology, sc-220452), 100 nM sodium orthovanadate (Alfa Aesar, 81104-14), 5 mM sodium fluoride (Sigma-Aldrich, S6776), 120 nM okadaic acid (EMD Millipore, 495604), PhosSTOP cocktail (Roche, 04906845001)) and ATP regeneration system (10 mM phosphocreatine (Sigma-Aldrich, P7936) and 0.45 mg ml^{-1} phosphocreatine kinase (Sigma-Aldrich, C3755)). Cells were ruptured by sonication using a Branson SFX150 Sonifier with a 3/32′ microtip at 68% power for four cycles consisting

of 15 s on and 30 s off. During the entire procedure, the microcentrifuge tubes with cell suspension were kept in ice-cold water. Ruptured cells were treated with 1 U μl⁻¹ OmniCleave endonuclease (Lucigen, OC7850K) for 5 min at 37 °C to release the DNA-bound protein pool, and cells were sonicated for one more cycle. The suspension was centrifuged at 4,000g for 15 min at 4 °C, supernatant was collected and the oligomers were pelleted by ultracentrifugation at 280,000g for 15 min at 4 °C. Pellets were washed three times by gently adding and removing of 100 μl lysis buffer supplemented with all components described above, CENP-T-based kinetochore-like particles were resuspended in 50 μl of the same buffer, immediately aliquoted and snap-frozen in liquid nitrogen for storage at −80 °C.

Determining the size of GFP-containing oligomers in vitro

Experiments were performed using a Nikon Eclipse Ti microscope equipped with 1.49× numerical aperture TIRF 100× oil objective. A CUBE 488-nm 100 mW diode laser (Coherent) provided excitation to visualize GFP-tagged proteins in TIRF mode. A CUBE 640-nm 50 mW diode laser and a CUBE 561-nm 100 mW diode laser (Coherent) provided excitation for microtubules polymerized from tubulins labelled with HiLyte647 or rhodamine. Images were acquired with an Andor iXon3 EMCCD camera and analysed using Fiji software[84]. The size of oligomers with the GFP-tagged proteins was determined by measuring their fluorescence intensity and dividing by the intensity of one GFP molecule, which was determined under identical imaging conditions.

First, to determine the brightness of a single GFP molecule, a flow chamber was incubated for 1 min with 100 pM recombinant 6His–GFP in Mg-BRB80 buffer (80 mM K-1,4-piperazinediethanesulfonic acid pH 6.9, 4 mM MgCl$_2$ and 1 mM EGTA). This protein was purified using a previously described protocol for His-tagged proteins described in ref. [15] (80 mM K-1,4-piperazinediethanesulfonic acid pH 6.9, 4 mM MgCl$_2$ and 1 mM EGTA). Next, the chamber was washed and sealed with VALAP (1:1:1 vaseline/lanolin/paraffin). Bleaching of individual GFP spots (Extended Data Fig. 3b) was captured for 1 min under TIRF illumination with 20% laser power and the following settings for Andor iXon3 camera: 1 MHz readout speed, gain 5.0×, EM (electron multiplying) gain 50, 300 ms exposure time. To take into account an unevenness of laser illumination, images of GFP molecules were normalized on the laser intensity profile, which was generated by averaging >100 images of randomly selected fields with GFP molecules at high density (1 nM GFP). An integral intensity of individual GFP molecules as a function of illumination time was measured in a circle area with the radius 3 pixels, generating individual photobleaching curves. Background intensity was measured in the same size area located near each GFP spot; individual background values were averaged for all examined spots, and the resultant curve was subtracted from the individual photobleaching curves. Further processing, such as smoothing with the sliding window of 4 points and curves alignment, was carried out, as in Volkov et al. 2014 (ref. [86]). Individual photobleaching curves were combined to build a histogram, in which the non-zero peak was fitted with Gaussian function to represent the mean value of single molecule intensity (Extended Data Fig. 3b).

Second, GFP-labelled oligomers isolated from mitotic cells were diluted 1,000–40,000 times in Mg-BRB80 buffer, flowed into the chamber and incubated for 5 min to immobilize them on the coverslip. Images were captured using the same camera settings as for single GFP molecules except the EM gain was decreased to 10. A linearity of EM gain settings was confirmed in separate experiments. Images of GFP-labelled oligomers were normalized on the laser intensity profile, and the oligomers were automatically selected using Fiji 'Find Maxima' plugin with 5,800 prominence level, which excluded small GFP-labelled oligomers. Finally, the integral intensity of individual oligomers and corresponding background were measured in a circle area with the radius 6 pixels. After background subtraction, number of GFP-tagged molecules per oligomer was calculated as a ratio of intensity of this oligomer divided by average intensity of single GFP molecule and multiplied by 5 to take into account difference in EM gain settings.

Assays with stabilized microtubules in vitro

Tubulin for microtubules was purified from cow brains by thermal cycling and chromatography[87], and labelled with HiLyte647 (HiLyte Fluor 647 succinimidyl ester; Anaspec, 81256), rhodamine (5-(and-6)-carboxytetramethylrhodamine succinimidyl ester; Invitrogen, C1171) or biotin (D-biotin succinimidyl ester; Invitrogen, B1513), as in previously described[88]. Taxol-stabilized fluorescent microtubules were prepared from a mixture of unlabelled and HiLyte647-labelled tubulin as in previously described[89] (9:1, total tubulin concentration 100 μM). Custom-made flow chambers were assembled with silanized coverslips (22 × 22 mm) using spacers made from two strips of double-sided sticky tape, as in Chakraborty et al. 2018 (ref. [89]). Solutions were perfused with syringe pump (New Era Pump Systems, cat. no. NE-4000), and all experiments were carried out at 32 °C. To immobilize taxol-stabilized microtubules, anti-tubulin antibodies (Serotec, MCA2047) were flowed into the chamber and the coverslip was blocked with 1% Pluronic F-127 (Sigma-Aldrich, CP2443) before introducing fluorescently labelled microtubules in Mg-BRB80 buffer supplemented with 7.5 μM taxol. Oligomers were then added in Imaging Buffer (Mg-BRB80 supplemented with 10 mM DTT, 7.5 μM taxol, 5 mM Mg-ATP, 4 mg ml⁻¹ BSA (Sigma-Aldrich, A7638), 0.1 mg ml⁻¹ casein (Sigma-Aldrich, C5890), 0.1 mg ml⁻¹ glucose oxidase (Sigma-Aldrich, G2133), 20 μg ml⁻¹ catalase (Sigma-Aldrich, C40) and 6 mg/ml glucose (Sigma-Aldrich, G8270), incubated for 5 min, and then GFP and microtubule images were collected in TIRF mode. To allow quantitative comparison of the level of microtubule decoration by different oligomers, care was taken to prepare solutions of clusters at similar concentration. To estimate concentration of isolated oligomers, thawed cluster suspensions were diluted 1,000–40,000-fold in Mg-BRB80 buffer and allowed to bind to the plasma cleaned coverslips for 5 min. Images of at least ten different microscopy fields were collected, and the number of clusters per field was determined. Concertation of oligomers was calculated as the average number of GFP-labelled oligomers per imaging field multiplied by the dilution factor. The concentration of CENP-T-based kinetochore-like particles was 10–20 times lower than preparations with control GFP oligomers, so the latter were diluted additionally to compensate for this difference. To quantify microtubule decoration with different oligomers, 10–20 rhodamine microtubules per imaging field were selected in the rhodamine channel. Then, the number of GFP-labelled oligomers co-localizing with these microtubules was determined in the GFP channel by automatic selection with Fiji 'Find Maxima' plugin with 5,800 prominence level.

Assays with dynamic microtubules in vitro

Microtubule seeds were prepared, as in Chakraborty et al. 2018 from a mixture of unlabelled, rhodamine- and biotin-labelled tubulins (8:1:1, total tubulin concentration 5 μM) supplemented with 1 mM GMPCPP (Jena Bioscience, NU-405L)[89]. A flow chamber was prepared as for assays with taxol-stabilized microtubules, but the coverslip was coated with 5 μM neutravidin to assist immobilization of the biotin-containing microtubule seeds. Imaging Buffer supplemented with 1 mM Mg-GTP, a mixture of unlabelled and HiLyte647-labelled tubulin (8:2, total tubulin concentration 5 μM) and up to 0.3% methyl cellulose was flowed using the pump. Microtubule growth was observed for 5 min, and then CENP-T-based kinetochore-like particles were flowed into the chamber. Imaging was carried out in TIRF mode switching between 488-nm and 640-nm lasers with 300 ms exposure using stream acquisition at 12 frames min⁻¹. To analyse tracking, a microtubule visible via Hilyte647 fluorescence was fitted with a straight line (5 pixels width) using Fiji software, and the kymograph in microtubule and GFP channels was prepared along this line. Kymographs with a bright GFP dot at the end of microtubule relative to lattice were scored as the tip-tracking

events. Polymerization and depolymerization microtubule rates were determined from the slopes of the corresponding kymographs.

Immunostaining of isolated CENP-T-based kinetochore-like particles

Immunostaining was performed on CENP-T-based kinetochore-like particles bound to taxol-stabilized microtubules or oligomers immobilized on the coverslips functionalized by 10-min incubation with 20 µg ml⁻¹ anti-S-tag antibodies (Abcam, ab87840) and blocked with 1% Pluronic F-127. Oligomers isolated from HeLa cells were allowed to adsorb onto the coverslip for 20 min. Chambers incubated with 3.5% paraformaldehyde or with no added fixative produced similar results, so these data were combined. Chambers were washed with Blocking Buffer (BRB80 buffer supplemented with 2 mM DTT, 4 mg ml⁻¹ BSA and 0.5 mg ml⁻¹ casein). Anti-Ndc80 antibodies diluted at 25 µg ml⁻¹ in Blocking Buffer were incubated for 15 min (ref. [51]), followed by Alexa647-conjugated anti-rabbit antibodies (1:100, Thermo Fisher Scientific, [A21245]) for 15 min, and washed with Imaging Buffer. To analyse level of Ndc80 recruitment, GFP-labelled oligomers were selected in GFP channel and the corresponding level of associated Ndc80 was measured as integral intensity in Alexa647 channel.

Single molecule assay to measure CENP-T–NDC80 binding in vitro

Flow chambers were prepared as described above in the section 'Assays with stabilized microtubules in vitro'. The surface of the coverslip was activated by incubation with 20 µg ml⁻¹ anti-S-tag antibodies (Abcam) diluted in BRB80 buffer for 10 min. The coverslip was blocked with 1% Pluronic F-127. Then, GFP–CENP-T$^{1-242/3D}$ or GFP oligomers were introduced to the flow chamber. The specimen on the microscope stage was maintained at 32 °C. The chamber was incubated for 20 min to allow immobilization of oligomers onto the coverslip. After immobilization oligomers were transferred to Imaging Buffer. Five images of the same field with GFP-tagged oligomers were collected for subsequent quantifications of their initial fluorescence intensity, which corresponds to the quantity of GFP–CENP-T$^{1-242/3D}$ or GFP molecules per oligomer. The oligomers were then bleached with a laser at 100% power for 30 s. Five images of the same field with oligomers were collected after bleaching to evaluate the efficiency of bleaching and the remaining GFP intensity of oligomers. Next, 100 µl of 100 nM GFP-tagged NDC80 in Imaging Buffer was introduced to the chamber using syringe pump at speed 900 µl min⁻¹. After 10 min, NDC80 was washed out from the chamber using 300 µl of Imaging Buffer perfused at speed 900 µl min⁻¹. Chamber was incubated for additional 10 min, and five images of the oligomers were collected to record recruitment of GFP-tagged NDC80.

The images were analysed using Fiji[84]. First, the image sequence was corrected on the stage drift using 'Manual drift correction' plugin. Then, the GFP intensity was measured in area surrounding the oligomer (8 pixels radius). Brightness of the same size area located near each oligomer was subtracted to minimize variability in background intensity. The intensities of individual oligomers during different stages of experiment were averaged between five frames. Final fluorescence intensity from GFP-tagged NDC80 was normalized on initial intensity from GFP–CENP-T$^{1-242/3D}$ or GFP oligomers. Resulting values represent average number of GFP-tagged NDC80 molecules per GFP–CENP-T$^{1-242/3D}$ or GFP molecule in oligomer.

The experiment with monomeric GFP–CENP-T$^{1-242/3D}$ was done analogously with several modifications. To obtain a field with evenly dispersed molecules, 0.25 nM GFP–CENP-T$^{1-242/3D}$ was used. GFP–CENP-T$^{1-242/3D}$ molecules were not photobleached, to avoid confusion between detached GFP–CENP-T$^{1-242/3D}$ molecules or those did not bind GFP-tagged NDC80. One frame was collected initially, and one was collected after NDC80 binding to avoid photobleaching. The probability of photobleaching was estimated from a photobleaching curve to be 4% over the 0.6-s exposure (Extended Data Fig. 9g). Smaller areas (3 pixels radius) surrounding GFP–CENP-T$^{1-242/3D}$ dots were used to measure their fluorescence intensity. To confirm, that GFP–CENP-T$^{1-242/3D}$ is monomeric, distribution of their initial fluorescence intensities was normalized to the fluorescence of one GFP molecule (Extended Data Fig. 9c).

Statistics and reproducibility

Statistical tests were performed in Prism (GraphPad) as described in figure legends. Detailed statistics are available in Source data. No statistical method was used to pre-determine sample size. No data were excluded from the analyses. The experiments were not randomized. The Investigators were not blinded to allocation during experiments and outcome assessment.

The results shown in western blots in Extended Data Fig. 6b,d,g,j were each repeated two times with similar results. The western blots in Extended Data Fig. 6e,f,k were cell line validation and control experiments that were performed only once. The western blot shown in Extended Data Fig. 6l was repeated three times with similar results. Information on replication for all other experiments can be found in figure legends.

Reporting summary

Further information on research design is available in Nature Portfolio Reporting Summary linked to this article.

Data availability

The proteomics data have been deposited to the ProteomeXchange Consortium via the PRIDE[90] partner repository with the dataset identifiers PXD042174 and https://doi.org/10.6019/PXD042174. Source data are provided with this paper. All other data supporting the findings of this study are available from the corresponding author on reasonable request.

References

77. Qian, K. et al. A simple and efficient system for regulating gene expression in human pluripotent stem cells and derivatives. *Stem Cells* **32**, 1230–1238 (2014).
78. Cong, L. et al. Multiplex genome engineering using CRISPR/Cas systems. *Science* **339**, 819–823 (2013).
79. Wang, T. et al. Identification and characterization of essential genes in the human genome. *Science* **350**, 1096–1101 (2015).
80. McKinley, K. L. & Cheeseman, I. M. Large-scale analysis of CRISPR/Cas9 cell-cycle knockouts reveals the diversity of p53-dependent responses to cell-cycle defects. *Dev. Cell* https://doi.org/10.1016/j.devcel.2017.01.012 (2017).
81. Welburn, J. P. I. et al. The human kinetochore Ska1 complex facilitates microtubule depolymerization-coupled motility. *Dev. Cell* **16**, 374–385 (2009).
82. Cheeseman, I. M. & Desai, A. A combined approach for the localization and tandem affinity purification of protein complexes from metazoans. *Sci. STKE* **2005**, 266 (2005).
83. Cheeseman, I. M. et al. KNL1 and the CENP-H/I/K complex coordinately direct kinetochore assembly in vertebrates. *Mol. Biol. Cell* **19**, 587–594 (2008).
84. Schindelin, J. et al. Fiji: an open-source platform for biological-image analysis. *Nat. Methods* **9**, 676–682 (2012).
85. Stirling, D. R. et al. CellProfiler 4: improvements in speed, utility and usability. *BMC Bioinform.* **22**, 1–11 (2021).
86. Volkov, V. A., Zaytsev, A. V. & Grishchuk, E. L. Preparation of segmented microtubules to study motions driven by the disassembling microtubule ends. *J. Vis. Exp.* **85**, 51150 (2014).
87. Miller, H. P. & Wilson, L. Preparation of microtubule protein and purified tubulin from bovine brain by cycles of assembly and disassembly and phosphocellulose chromatography. *Methods Cell Biol.* **95**, 2–15 (2010).

88. Hyman, A. A. & Mitchison, T. J. Two different microtubule-based motor activities with opposite polarities in kinetochores. *Nature* **351**, 206–211 (1991).

89. Chakraborty, M., Tarasovetc, E. V. & Grishchuk, E. L. in *Mitosis and Meiosis Part A* (eds Maiato, H. & Schuh, M.) Ch. 13 (2018).

90. Perez-Riverol, Y. et al. The PRIDE database resources in 2022: a hub for mass spectrometry-based proteomics evidences. *Nucleic Acids Res.* **50**, D543–D552 (2022).

Author contributions

Conceptualization—G.B.S., I.M.C. and E.L.G.; methodology, validation and investigation—G.B.S. for reagent generation, experimental design and all in vivo experiments, E.V.T. for all in vitro experiments, and O.M. for western blots and additional support; writing, original draft preparation—G.B.S. and I.M.C.; writing, review and editing—E.L.G., E.V.T. and O.M.; visualization—G.B.S., E.V.T. and O.M.; supervision—I.M.C. and E.L.G.; funding acquisition—I.M.C. and E.L.G.

Competing interests

The authors declare no competing interests.

Additional information

Extended data is available for this paper at https://doi.org/10.1038/s41556-023-01313-7.

Supplementary information The online version contains supplementary material available at https://doi.org/10.1038/s41556-023-01313-7.

Correspondence and requests for materials should be addressed to Ekaterina L. Grishchuk or Iain M. Cheeseman.

Peer review information *Nature Cell Biology* thanks Kerry Bloom and the other, anonymous, reviewer(s) for their contribution to the peer review of this work. Peer reviewer reports are available.

Reprints and permissions information is available at www.nature.com/reprints.
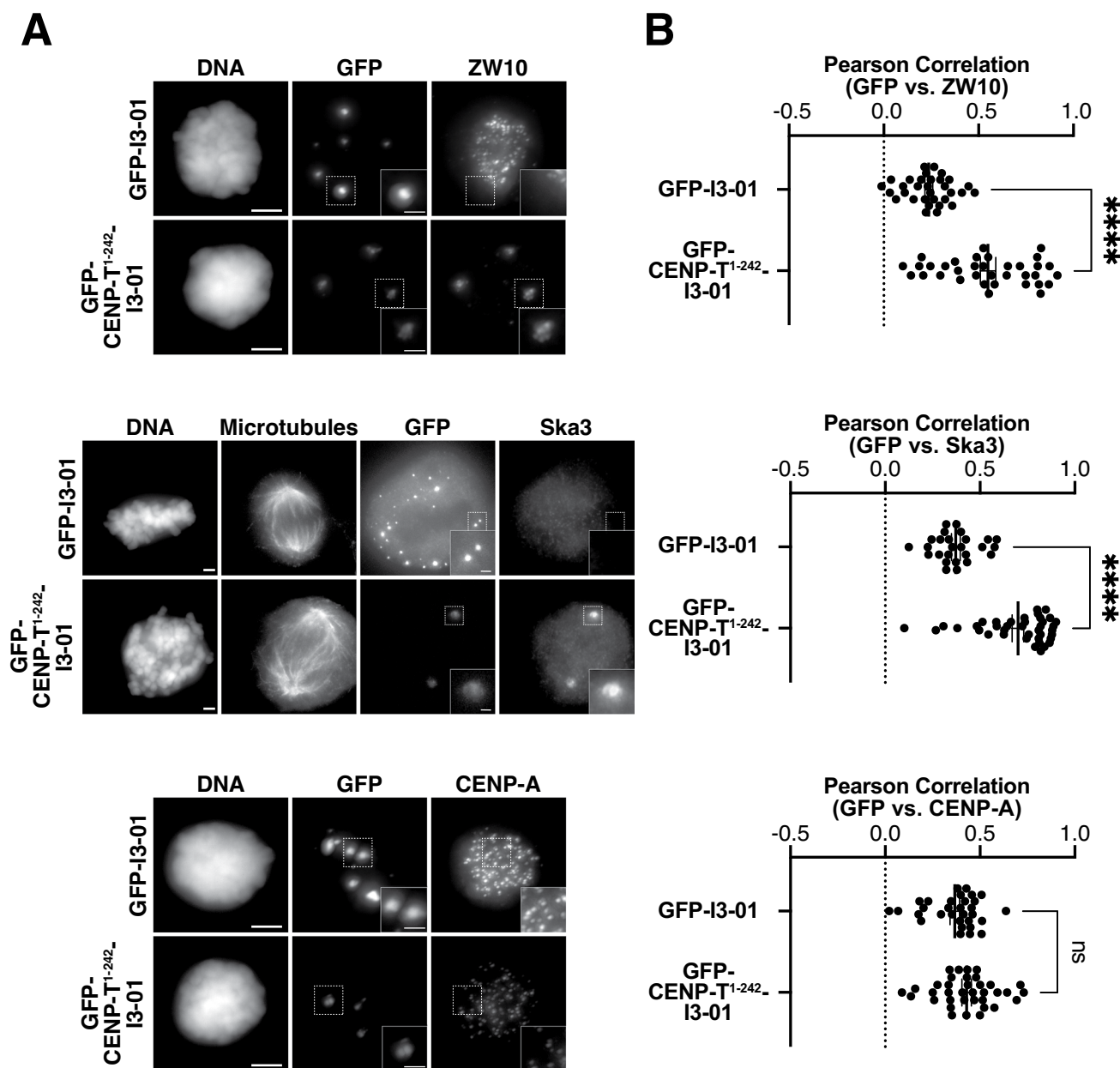
Extended Data Fig. 1 | CENP-T$^{1-242}$ oligomers interact with spindles and recruit additional outer kinetochore proteins, but control oligomers do not. (a) Co-localization of outer kinetochore proteins with GFP-CENP-T$^{1-242}$-I3-01 oligomers by immunofluorescence. Identical linear brightness adjustments were used for GFP and kinetochore protein channels for each pair of experimental and control samples. Regions enlarged in insets are indicated by dashed boxes. Full-size image scale bars=5 μm. Inset scale bars=2 μm. SKA3 experiment was repeated 4 times with similar results. CENP-A and ZW10 experiments were repeated twice

with similar results. **(b)** Pearson correlations between GFP and kinetochore protein signals for GFP-I3-01 and GFP-CENP-T$^{1-242}$-I3-01. Each point is a cell; n=number of cells measured in a single experiment. Bars represent mean ± SEM.; each experiment was performed 2 times with similar results. Statistical analysis of replicates and sample sizes can be found in Supplementary Table 4. P-values were calculated with Welch's two-tailed t-tests: ZW10: $p < 0.0001$; SKA3: $p < 0.0001$; CENPA: $p = 0.0809$. Source numerical data are available in Source Data.

A

IP-Mass Spectrometry GFP-I3-01

		Coverage (%)	Peptides	PSMs		Coverage (%)	Peptides	PSMs	
Bait	CENP-T$^{1\text{-}242}$	4	1	2	ZW10	-	-	-	**RZZ Complex**
	GFP	42	13	458	Rod	-	-	-	
	I3-01	38	13	216	Zwilch	-	-	-	
NDC80 Complex	NDC80	-	-	-	Ska1	-	-	-	**Ska1 Complex**
	Nuf2	-	-	-	Ska2	-	-	-	
	Spc24	-	-	-	Ska3	-	-	-	
	Spc25	-	-	-	Astrin	-	-	-	**Astrin-SKAP Complex**
MIS12 Complex	Dsn1	-	-	-	SKAP	22	6	29	
	Mis12	-	-	-	MYCBP	-	-	-	
	Nsl1	-	-	-	LC8	-	-	-	
	Pmf1	-	-	-	Bub1	-	-	-	**Other**
KNL1 Complex	Knl1	-	-	-	Bub3	-	-	-	
	ZWINT	20	5	8	Mad2L1	-	-	-	
					Spindly	-	-	-	
					chTOG	-	-	-	

B

IP-Mass Spectrometry

	GFP-CENP-T$^{1\text{-}242}$-I3-01			GFP-I3-01		
	Coverage (%)	Peptides	PSMs	Coverage (%)	Peptides	PSMs
CENP-A	-	-	-	-	-	-
CENP-B	2	1	2	-	-	-
CENP-C	-	-	-	-	-	-
CENP-L	-	-	-	-	-	-
CENP-N	-	-	-	-	-	-
CENP-H	11	2	3	-	-	-
CENP-I	-	-	-	-	-	-
CENP-K	4	1	1	-	-	-
CENP-M	6	1	2	-	-	-
CENP-O	-	-	-	-	-	-
CENP-P	-	-	-	-	-	-
CENP-Q	-	-	-	-	-	-
CENP-U	-	-	-	-	-	-
CENP-R	-	-	-	-	-	-
CENP-W	-	-	-	-	-	-
CENP-S	13	2	3	-	-	-
CENP-X	-	-	-	-	-	-

Extended Data Fig. 2 | CENP-T$^{1\text{-}242}$ oligomers recruit additional outer kinetochore proteins, but control oligomers do not. (a) Outer kinetochore and kinetochore-associated proteins detected in immuno-precipitation mass spectrometry of GFP-I3-01 control oligomers. This experiment was performed twice with similar results. **(b)** Peptides counts for inner kinetochore proteins detected in immunoprecipitation mass spectrometry of GFP-I3-01 and GFP-CENP-T$^{1\text{-}242}$-I3-01 oligomers. This experiment was performed twice with similar results.
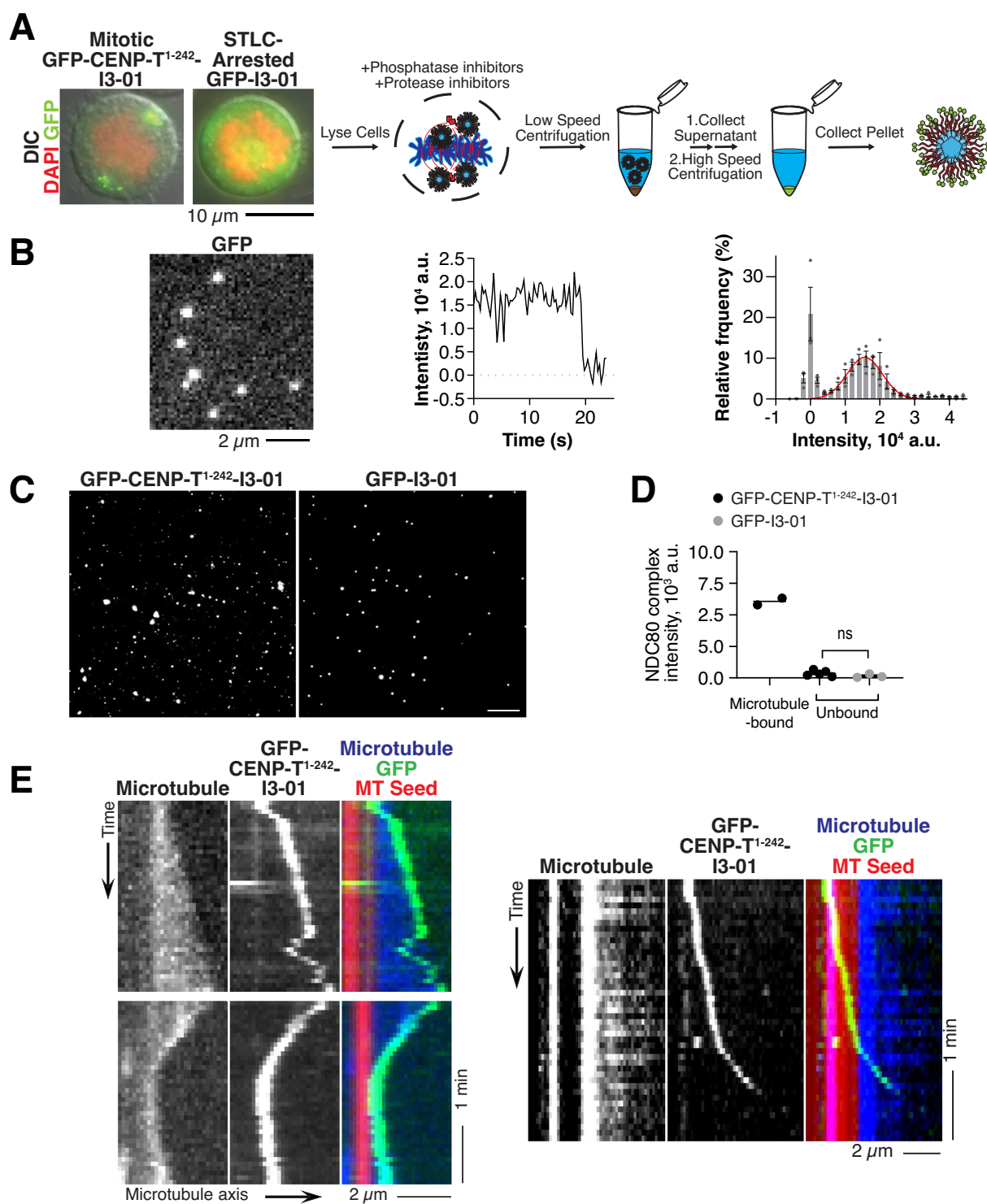
**Extended Data Fig. 3 | See next page for caption.**

Extended Data Fig. 3 | Characterization of GFP CENP-T$^{1-242}$ and control GFP oligomers isolated from HeLa cells. (a) Workflow to isolate GFP-CENP-T$^{1-242}$-I3-01 and GFP-I3-01 from mitotic cells. Left: representative images of HeLa cells expressing GFP-CENP-T$^{1-242}$ or GFP oligomers. Cells were arrested in mitosis by expression of GFP-CENP-T$^{1-242}$-I3-01 or with the Eg5 inhibitor S-Trityl-L-Cysteine (see Methods for details). **(b)** Quantification of the number of GFP molecules. Left: representative image of a microscope field with single GFP molecules immobilized on plasma-cleaned coverslip. Repeated 3 times with similar results. Middle: Example photobleaching curve for a single molecule of GFP. Right: Histogram of integral intensities collected from 60 bleaching GFP dots from N = 3 independent experiments. Each point represents the frequency in one independent repeat. Red line is fit to Gaussian function. Bars represent mean ± SEM. Peak value of $1.56 \pm 0.04 \times 10^4$ a.u. is the integral intensity of a single GFP fluorophore under our imaging conditions. This intensity was used to estimate number of GFP fluorophores in oligomers and complexes, see Methods for details. **(c)** Representative fluorescence microscopy images of the indicated GFP-labelled oligomers immobilized on coverslips; identical microscopy settings and brightness adjustments were used. Repeated 5 times with similar results. **(d)** Immunofluorescence measurements of NDC80 intensity associated with CENP-T$^{1-242}$ oligomers and GFP oligomers that bound to taxol-stabilized microtubules or did not bind to microtubules. Each point represents the median value from an independent experiment. Bars represent mean ± SEM. For microtubule-bound GFP-CENP-T$^{1-242}$-I3-01, N = 2; for other conditions N = 5. Two-tailed Welch's t-test: GFP-CENP-T$^{1-242}$-I3-01 unbound vs. GFP-I3-01 unbound: p = 0.2129. **(e)** Kymographs illustrating complex motions of CENP-T$^{1-242}$ oligomers on dynamic microtubules. Top left: an CENP-T$^{1-242}$ oligomer diffuses on the microtubule wall and tracks the polymerizing plus-end. Bottom left: CENP-T$^{1-242}$ oligomer tracks a depolymerize end, then tracks the end when it reverts to polymerization. Right: Processive plus-end-directed movement. Velocity on the GMPCPP-containing seed (red): 0.7 µm/min; on GDP-containing lattice (blue) 3 µm/min. Plus-end directed motion was observed in 8 out of 80 total observations. Observations were made over 8 independent experiments. Source numerical data are available in Source Data.
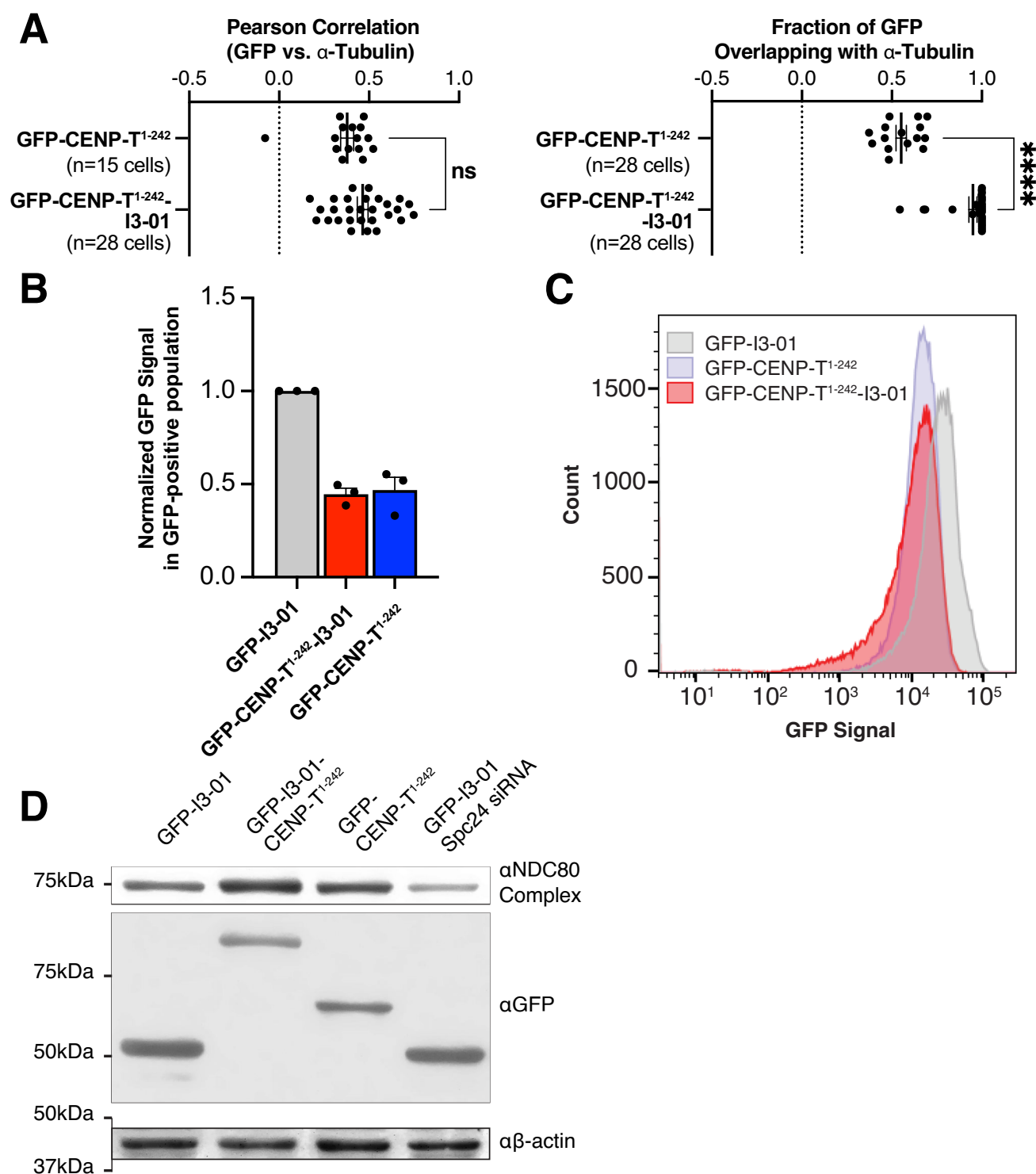
Extended Data Fig. 4 | CENP-T$^{1-242}$ oligomers and monomers have distinct localization, are expressed at comparable levels, and do not reduce outer kinetochore protein expression. (a) Pearson correlation and Manders overlap coefficient for GFP and α-tubulin co-localization in cells expressing GFP-CENP-T$^{1-242}$ or GFP-CENP-T$^{1-242}$-I3-01. Datapoints are cells from a single experiment. Bars represent mean ± SEM. Each experiment was performed 2 times with similar results. Statistical analysis of replicates can be found in Supplementary Table 4. Two-tailed Welch's t-tests: Pearson correlation: p = 0.0793; Overlap: p < 0.0001. **(b)** Normalized GFP signals from GFP-positive cells analyzed for DNA content in Fig. 4e as measured by flow cytometry. Each point is the mean GFP signal from 3 independent experiments. Bars represent

mean ± SEM. The same cell lines were used for other assays with these three constructs. **(c)** Histograms showing the distribution of GFP expression levels in cells from cell line in **(b)** as measured by flow cytometry. Repeated 3 times with similar results. **(d)** Western Blot for expression levels of the NDC80 complex component NDC80 in cells expressing different constructs. NDC80 was detected using an antibody against the whole complex. Anti-GFP antibody was used to show expression of the expected construct in each cell line. Beta-Actin was used as a loading control. The NDC80 complex is an obligate complex, so depletion of one component, Spc24, with siRNA resulted in a reduction in NDC80 levels. This experiment was repeated 3 times with similar results. Source numerical data and unprocessed blots are available in Source Data.
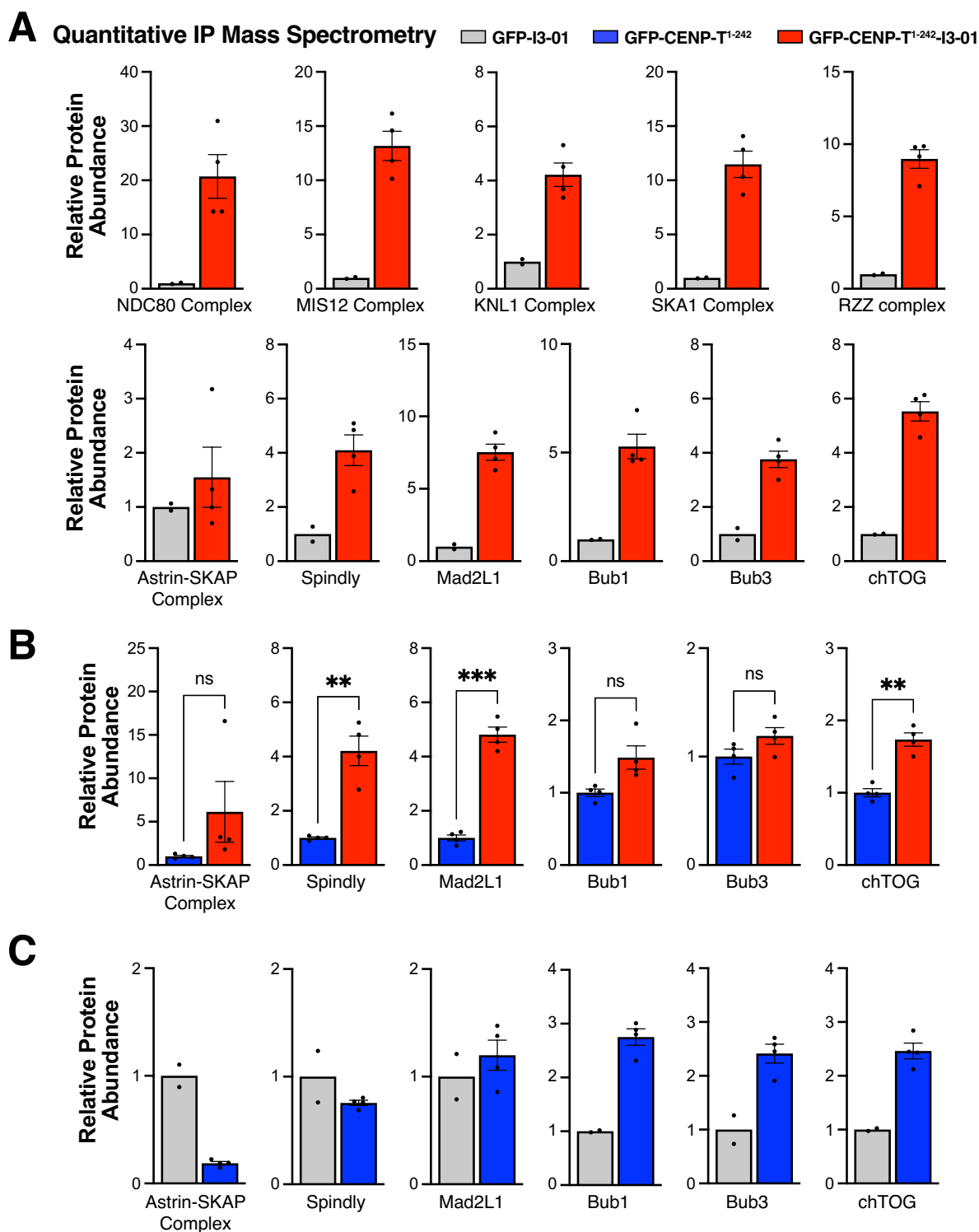
Extended Data Fig. 5 | CENP-T$^{1-242}$ oligomers recruit kinetochore-associated proteins and spindle assembly checkpoint proteins more robustly than monomeric CENP-T$^{1-242}$. (a) Comparison of protein co-immunoprecipitation by CENP-T$^{1-242}$ oligomers and control GFP oligomers by quantitative mass spectrometry. Each point represents a biological replicate from a single multiplexed mass spectrometry run. Bars represent mean ± SEM. Analysis details can be found in Methods. **(b)** Comparison of protein co-immuno-precipitation by CENP-T$^{1-242}$ oligomers and CENP-T$^{1-242}$ monomers by TMT-based quantitative immune-precipitation mass spectrometry. Presented and analyzed as described in **(a)**. Two-tailed Welch's t-test: Astrin-SKAP: $p = 0.2383$; Spindly: $p = 0.0094$; Mad2L1: $p = 0.0002$; Bub1: $p = 0.0506$; Bub3: $p = 0.1151$; chTOG: $p = 0.001$. **(c)** Comparison of protein co-immuno-precipitation by control GFP oligomers and CENP-T$^{1-242}$ monomers by TMT-based quantitative immuno-precipitation mass spectrometry. Presented and analyzed as described in **(a)**. Source numerical data are available in Source Data.
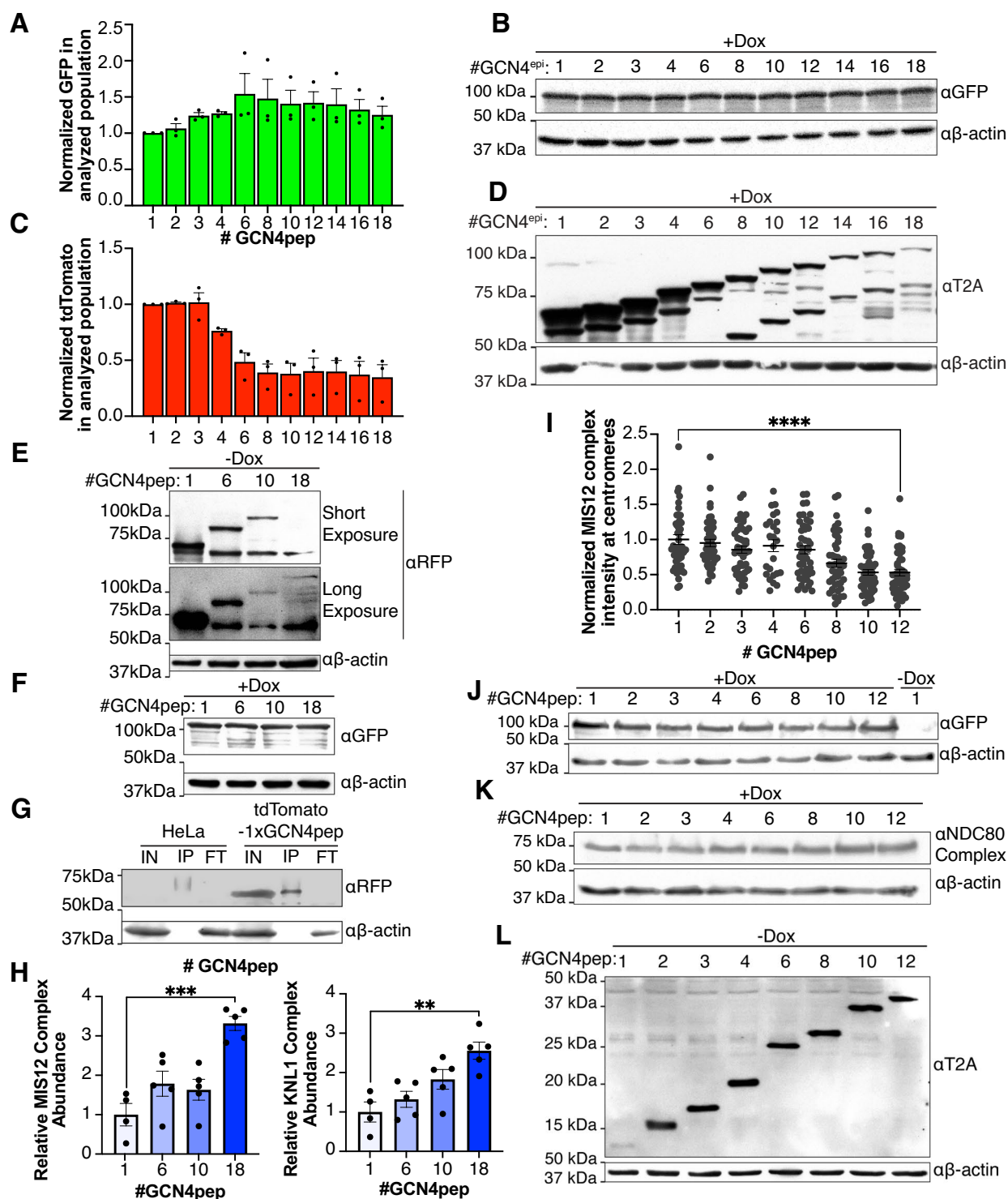
Extended Data Fig. 6 | See next page for caption.

Extended Data Fig. 6 | Additional SunTag mass spectrometry, centromere depletion, and controls. (a) Normalized GFP signals from SunTag cells in Fig. 5c as measured by flow cytometry. Each point is the mean from N = 3 independent experiments. Bars represent mean ± SEM. **(b)** Anti-GFP western blot of cell lines expressing scFv-sfGFP-CENP-T$^{1-242}$ with different tdTomato-tagged GCN4pep scaffolds. β-Actin was used as a loading control here and in all subsequent western blots. **(c)** Same analysis as in **(a)** for tdTomato. **(d)** Anti-T2A western blots of SunTag cell lines with different tdTomato-tagged GCN4pep scaffolds. Anti-T2A antibody binds to the C-terminus of the scaffolds. Experiments in panels **(a-d)** were performed on cells from Fig. 5c. **(e)** and **(f)** Anti-RFP and Anti-GFP westerns blots of SunTag cell lines expressing tdTomato-tagged GCN4pep scaffolds used in Fig. 5d, Extended Data Fig. 6h. **(g)** Validation western of anti-mCherry antibodies for immunoprecitation. IN=Input, IP=Immunoprecipitation, FT=Flow-through. **(h)** Comparison of MIS12 and KNL1 complex abundances in anti-mCherry quantitative immunoprecipitation mass spectrometry with different SunTag scaffolds. Each point represents a biological replicate from 2 multiplexed experiments. Each bar represents the mean ± SEM Two-tailed Welch's t-test: MIS12: 1 vs. 6: p = 0.1083; 6 vs. 10: p = 0.7135; 10 vs. 18: p = 0.0011; 1 vs. 18: p = 0.0008. KNL1: 1 vs. 6: p = 0.3592; 6 vs. 10: p = 0.1559; 10 vs. 18: p = 0.0605; 1 vs. 18: p = 0.003. **(i)** Quantification of MIS12 levels at centromeres in cells expressing the scFv-sfGFP-CENP-T$^{1-242}$ with different GCN4pep scaffolds. Each point is a cell. Each bar represents the mean ± SEM. Measurements were pooled from 3 independent experiments. 1: n = 49; 2: n = 45; 3: n = 47; 4: n = 25; 6: n = 47; 8: n = 47; 10: n = 51; 12: n = 47. Two-tailed Welch's t test: 1 v. 12: p < 0.0001. Welch's ANOVA test: P < 0.0001. **(j)** and **(k)** Anti-NDC80 Complex and anti-GFP western blots of SunTag cell lines expressing scFv-sfGFP-CENP-T$^{1-242}$ alongside different GCN4pep scaffolds. **(l)** Same as in **(d)**. Experiments in panels (J-L) were performed on cells lines used in Fig. 5e, f, Extended Data Fig. 6i. Scaffolds in these cell lines lack the tdTomato tag. Source numerical data and unprocessed blots are available in Source Data.

DNA content Analysis gating strategy for Figure 5C
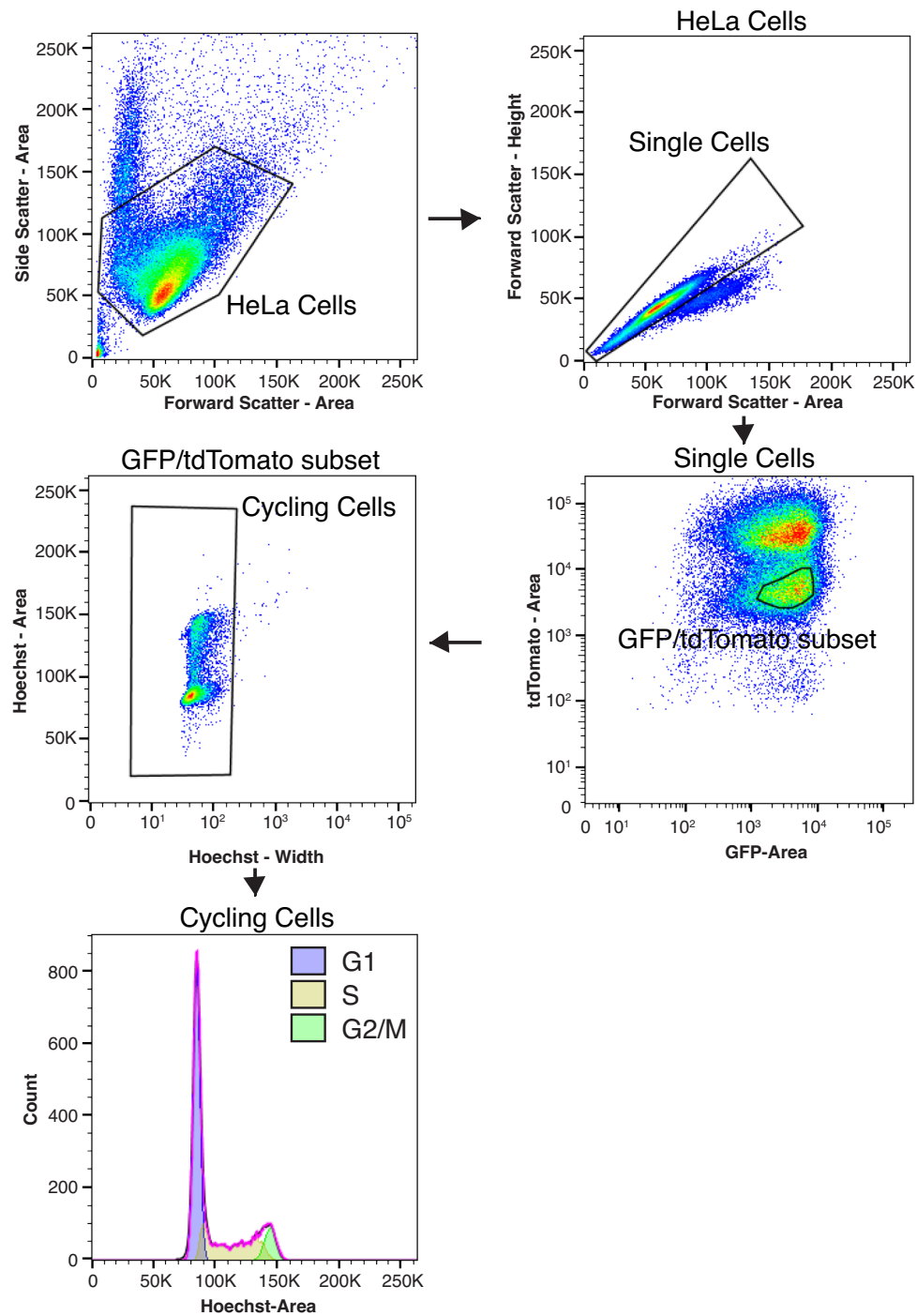
Extended Data Fig. 7 | Flowcytometry gating strategy for DNA content analysis of CENP-T[1-242] SunTag oligomers. Gating strategy to select the population of cells to be analyzed for DNA content analysis in Fig. 5c. A similar gating strategy was used in Fig. 4e without the tdTomato-Area parameter.

A

B

C

D
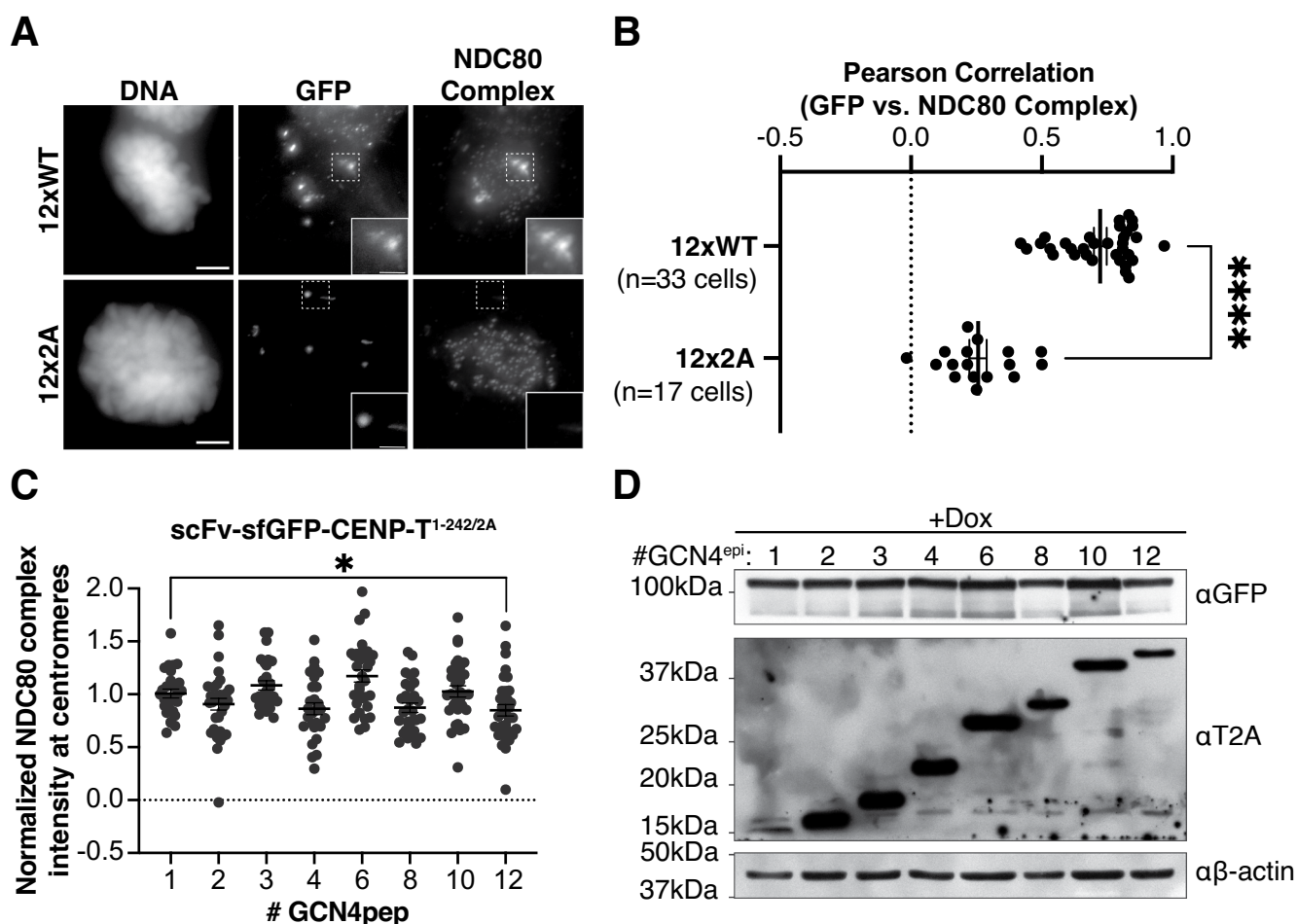
Extended Data Fig. 8 | Known N-terminal NDC80 phosphorylation sites are required for NDC80 recruitment to oligomers. (a) Representative images of colocalization of GFP and the NDC80 complex in cells expressing scFv-sfGFP-CENP-T$^{1-242}$ with either wild-type (WT) CENP-T$^{1-242}$ or CENP-T$^{1-242}$ with T11A and T85A mutations (2 A). These constructs were expressed alongside 12xGCN4pep scaffolds. **(b)** Pearson correlations between GFP and NDC80 signal for experiment in **(a)**. Datapoints are cells from a single experiment. Bars represent mean ± SEM. Repeated 2 times with similar results. Statistical analysis of replicates and sample sizes can be found in Source Data. Two-tailed Welch's t-test: p < 0.0001. **(c)** Quantification of NDC80 levels at centromeres in cells expressing scFv-sfGFP-CENP-T$^{1-242/2A}$ with different GCN4pep scaffolds. Each bar represents

the mean ± SEM of NDC80 signal from cells expressing the designated construct. Measurements were pooled from 2 different experiments. n=number of cells pooled from 2 independent experiments. 1: n = 27; 2: n = 33; 3: n = 28; 4: n = 27; 6: n = 31; 8: n = 30; 10: n = 31; 12: n = 33. Welch's ANOVA: p < 0.0001. Two-tailed Welch's t-test: 1 v. 12: p = 0.0237. **(d)** Anti-GFP and Anti-T2A western blots of cell lines expressing different GCN4pep scaffolds alongside scFv-sfGFP-CENP-T$^{1-242/2A}$. Anti-T2A antibody binds to the C-terminus of the scaffolds. β-Actin was used as a loading control. These cell lines were used in for all experiments in the figure. This was a cell line validation experiment that was only performed once. Source numerical data and unprocessed blots are available in Source Data.
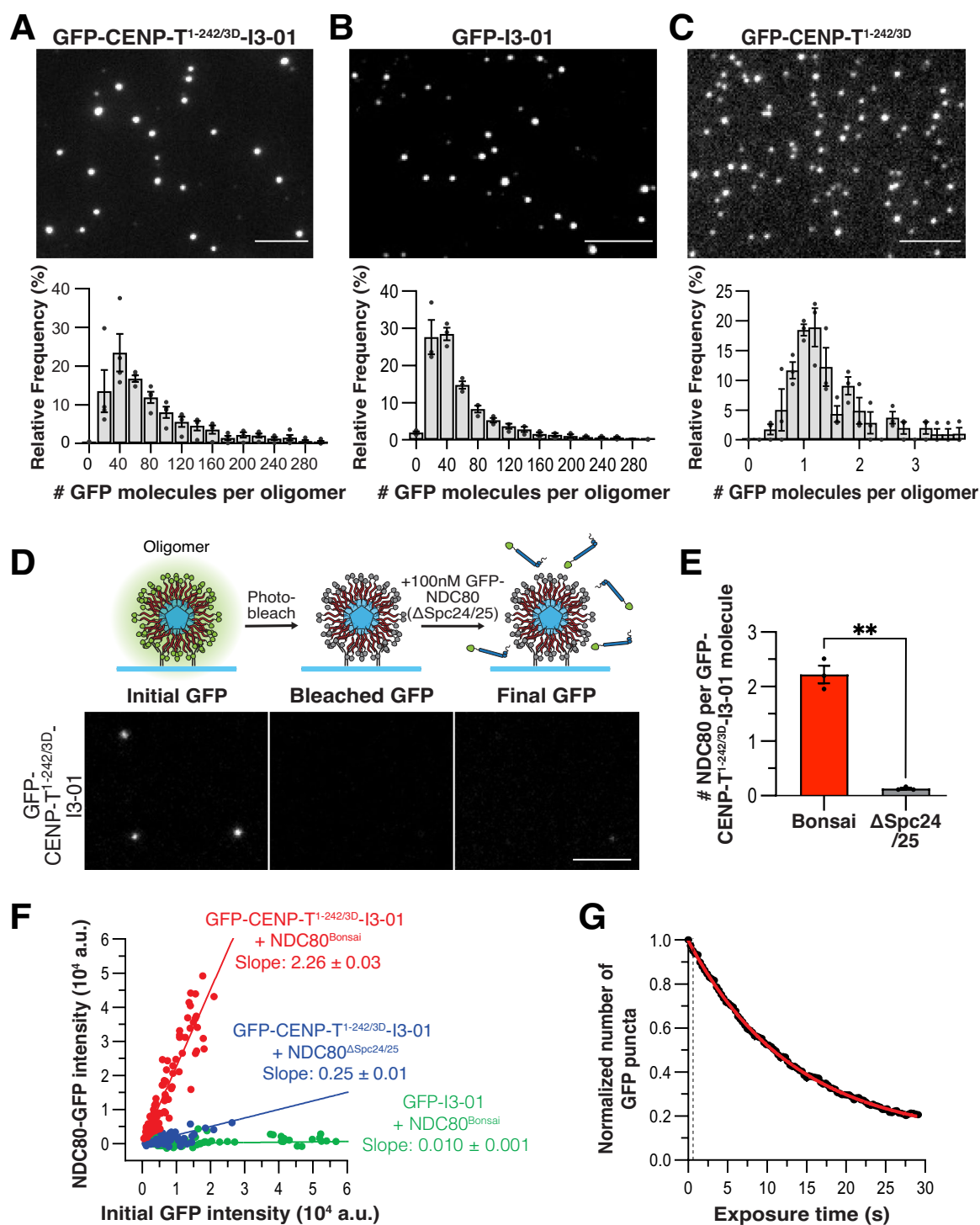
Extended Data Fig. 9 | See next page for caption.

Extended Data Fig. 9 | Additional fluorescence intensity quantifications for *in vitro* CENP-T-NDC80 binding assay using recombinant oligomers and NDC80 proteins. (a) Top: Representative images of purified recombinant GFP-CENP-T$^{1-242/3D}$-I3-01 oligomers attached to a coverslip. Bottom: histogram of the distribution of the number of GFP molecules per oligomer as a percentage of the total number of examined oligomers. Each point represents an independent measurement. Each bar represents the mean ± SEM from 3 independent experiments. Distribution mean ± SEM: 66 ± 10 GFP molecules. **(b)** Same as **(a)** for GFP-I3-01. 3 independent experiments. Distribution mean ± SEM: 44 ± 4 GFP molecules. **(c)** Same as **(a)** for GFP-CENP-T$^{1-242/3D}$. 3 independent experiments. Distribution mean ± SEM: 1.23 ± 0.05 molecules. **(d)** Single molecule binding experiment with NDC80$^{\Delta Spc24/25}$. Top: Experimental workflow. Bottom: representative images of GFP-CENP-T$^{1-242/3TD}$-I3-01 oligomers at each experimental stage. **(e)** Efficiency of NDC80^{Bonsai} or NDC80$^{\Delta Spc24/25}$ recruitment to GFP-CENP-T$^{1-242/3D}$-I3-01 oligomers. Bars represent mean ± SEM. Each point is the median result from 3 independent experiments with >12 oligomers. Data for GFP-CENP-T$^{1-242/3D}$-I3-01 oligomer is duplicated from Fig. 6d. Two-tailed Welch's

t-test: p = 0.0054. **(f)** Graph of the stoichiometry of binding. Final GFP signal intensity as function of initial GFP signal intensity for individual oligomers. Each point represents the measurement for one oligomer pooled from N = 3 independent experiments per data set. GFP-CENP-T$^{1-242/3D}$-I3-01+NDC80^{Bonsai}: n = 85 Oligomers; GFP-CENP-T$^{1-242/3D}$-I3-01 + NDC80$^{\Delta Spc24/25}$: n = 79 Oligomers; GFP-I3-01+NDC80^{Bonsai}: n = 91 Oligomers. Data are fitted to linear functions. The slopes (± standard fitting error) correspond to the number of NDC80 molecules recruited per GFP-containing monomer for each combination of oligomer and NDC80 complex. **(g)** Photobleaching curve taken with identical microscope settings to those used for experiments with GFP-CENP-T$^{1-242/3D}$ (Fig. 6b, e, f). The number of GFP puncta per imaging field at each time point was normalized to the number at t = 0. Data were fitted to an exponential decay function to estimate the probability of bleaching during imaging time. Each point represents the mean ± SEM from N = 3 independent measurements. Dashed line indicates experimental exposure time in Fig. 6e, f. Source numerical data are available in source data.

Corresponding author(s): Iain Cheeseman and Ekaterina Grishchuk

Last updated by author(s): Nov 4, 2023

Reporting Summary

Nature Portfolio wishes to improve the reproducibility of the work that we publish. This form provides structure for consistency and transparency in reporting. For further information on Nature Portfolio policies, see our Editorial Policies and the Editorial Policy Checklist.

Statistics

For all statistical analyses, confirm that the following items are present in the figure legend, table legend, main text, or Methods section.

n/a	Confirmed	
☐	☒	The exact sample size (*n*) for each experimental group/condition, given as a discrete number and unit of measurement
☐	☒	A statement on whether measurements were taken from distinct samples or whether the same sample was measured repeatedly
☐	☒	The statistical test(s) used AND whether they are one- or two-sided *Only common tests should be described solely by name; describe more complex techniques in the Methods section.*
☒	☐	A description of all covariates tested
☒	☐	A description of any assumptions or corrections, such as tests of normality and adjustment for multiple comparisons
☐	☒	A full description of the statistical parameters including central tendency (e.g. means) or other basic estimates (e.g. regression coefficient) AND variation (e.g. standard deviation) or associated estimates of uncertainty (e.g. confidence intervals)
☐	☒	For null hypothesis testing, the test statistic (e.g. *F*, *t*, *r*) with confidence intervals, effect sizes, degrees of freedom and *P* value noted *Give P values as exact values whenever suitable.*
☒	☐	For Bayesian analysis, information on the choice of priors and Markov chain Monte Carlo settings
☒	☐	For hierarchical and complex designs, identification of the appropriate level for tests and full reporting of outcomes
☒	☐	Estimates of effect sizes (e.g. Cohen's *d*, Pearson's *r*), indicating how they were calculated

Our web collection on statistics for biologists contains articles on many of the points above.

Software and code

Policy information about availability of computer code

Data collection	BD FACSdiva was used to collect flow cytometry data. Softworx, AcquireUltra, and Nikon NIS-Elements Software (version 4.30.02) were used to collect imaging data.
Data analysis	Cell Profiler 4.0 was used to measure the intensity of kinetochore proteins at centromeres. Prism 8, 9, and 10 were used for statistical analyses and data presentation. Image analysis was performed in FIJI/ImageJ2. FlowJo 9 and 10 were used for DNA content analyses and to measure the fluorescence intensities of cells expressing our constructs. Proteome Discoverer 2.4 was used to analyze raw mass spectrometry data.

For manuscripts utilizing custom algorithms or software that are central to the research but not yet described in published literature, software must be made available to editors and reviewers. We strongly encourage code deposition in a community repository (e.g. GitHub). See the Nature Portfolio guidelines for submitting code & software for further information.

Data

Policy information about availability of data

All manuscripts must include a data availability statement. This statement should provide the following information, where applicable:

- Accession codes, unique identifiers, or web links for publicly available datasets
- A description of any restrictions on data availability
- For clinical datasets or third party data, please ensure that the statement adheres to our policy

> The data that support the findings of this study are available from the corresponding author upon reasonable request. We are working on uploading proteomics data, which will be available prior to publication.

Research involving human participants, their data, or biological material

Policy information about studies with human participants or human data. See also policy information about sex, gender (identity/presentation), and sexual orientation and race, ethnicity and racism.

Reporting on sex and gender	*Use the terms sex (biological attribute) and gender (shaped by social and cultural circumstances) carefully in order to avoid confusing both terms. Indicate if findings apply to only one sex or gender; describe whether sex and gender were considered in study design; whether sex and/or gender was determined based on self-reporting or assigned and methods used. Provide in the source data disaggregated sex and gender data, where this information has been collected, and if consent has been obtained for sharing of individual-level data; provide overall numbers in this Reporting Summary. Please state if this information has not been collected. Report sex- and gender-based analyses where performed, justify reasons for lack of sex- and gender-based analysis.*
Reporting on race, ethnicity, or other socially relevant groupings	*Please specify the socially constructed or socially relevant categorization variable(s) used in your manuscript and explain why they were used. Please note that such variables should not be used as proxies for other socially constructed/relevant variables (for example, race/ethnicity should not be used as a proxy for socioeconomic status). Provide clear definitions of the relevant terms used, how they were provided (by the participants/respondents, the researchers, or third parties), and the method(s) used to classify people into the different categories (e.g. self-report, census or administrative data, social media data, etc.) Please provide details about how you controlled for confounding variables in your analyses.*
Population characteristics	*Describe the covariate-relevant population characteristics of the human research participants (e.g. age, genotypic information, past and current diagnosis and treatment categories). If you filled out the behavioural & social sciences study design questions and have nothing to add here, write "See above."*
Recruitment	*Describe how participants were recruited. Outline any potential self-selection bias or other biases that may be present and how these are likely to impact results.*
Ethics oversight	*Identify the organization(s) that approved the study protocol.*

Note that full information on the approval of the study protocol must also be provided in the manuscript.

Field-specific reporting

Please select the one below that is the best fit for your research. If you are not sure, read the appropriate sections before making your selection.

[X] Life sciences   [ ] Behavioural & social sciences   [ ] Ecological, evolutionary & environmental sciences

For a reference copy of the document with all sections, see nature.com/documents/nr-reporting-summary-flat.pdf

Life sciences study design

All studies must disclose on these points even when the disclosure is negative.

Sample size	For measurement of kinetochore protein levels at centromeres, 15 mitotic cells or the maximum number of mitotic cells that could be distinguished in 7-10 images were used. For each condition for each experiment. Data were normalized and pooled from multiple experiments to increase sample sizes. The final sample sizes were sufficient to identify differences with high levels of statistical significance. For colocalization analyses, sample sizes can be found in Source Data. For Flowcytometry experiments, 50,000 single cells were recorded for each experiments. Cell cycle analysis was performed on a subset of these (see Extended Data Figure 7).
Data exclusions	No data were excluded from our analyses
Replication	Except for quantitative mass spectrometry experiments, all experiments were replicated at least twice with the same or similar results. For quantitative mass spectrometry experiments, multiple biological replicates were used for each condition (replicates are shown as datapoints in figures). Biological replicates were from populations of cells that were grown separately for at least 1.5 weeks prior to harvesting.

Randomization	This study was performed entirely using cell lines expressing different constructs or constructs purified from specific cell lines/bacteria, so randomization was not relevant. Experimental groups were assessed in the same experiments as control groups.
Blinding	Investigators were not blinded to group allocation during the collection of data. For the measurements of kinetochore protein levels at kinetochores and colocalization, this was not relevant because mitotic cells were identified for imaging by scanning the plate in the Hoechst channel (DNA dye), which did not give information on the levels of kinetochore proteins at centromeres. Because measurements were performed by Cell Profiler 4.0 software, there were no biases in the measurements. Similarly, measurements of the fractions of cells in G2/M were made using mathematical models in FlowJo, so biases are unlikely. For images of cells and preparation of samples for mass spectrometry, all experiments were performed by GBS, who also made and numbered all cell lines, so blinding was not practical.

Reporting for specific materials, systems and methods

We require information from authors about some types of materials, experimental systems and methods used in many studies. Here, indicate whether each material, system or method listed is relevant to your study. If you are not sure if a list item applies to your research, read the appropriate section before selecting a response.

Materials & experimental systems

n/a	Involved in the study
☐	☒ Antibodies
☐	☒ Eukaryotic cell lines
☒	☐ Palaeontology and archaeology
☒	☐ Animals and other organisms
☒	☐ Clinical data
☒	☐ Dual use research of concern
☒	☐ Plants

Methods

n/a	Involved in the study
☐	☐ ChIP-seq
☐	☒ Flow cytometry
☐	☐ MRI-based neuroimaging

Antibodies

Antibodies used	See Supplementary table 2.
Validation	1. anti-Tubulin Beta 3 antibody (Serotec, MCA2047) - the manufacturer reported that the product works in the following applications: Immunohistology, Western Blotting, Immunofluorescence . Target Species: Human; Species Cross Reactivity, reacts with: Mouse, Baboon, Rat, Hamster, Pig, Bovine. Refs: Dráberová, E. et al. (1998) Histochem Cell Biol; Hattermann, K. et al. (2010) Cancer Res; Rosito, M. et al. (2012) . J Neurosci; Nicot, A. and DiCicco-Bloom, E. (2001). Proc Natl Acad Sci U S A; Pěknicová, J. et al. (2001). Biol Reprod; Huang, C.L. et al. (2010) Exp Ther Med.

2. anti-alpha-tubulin antibody (Sigma-Aldrich, T9026): Manufacturer states that "Mouse monoclonal specifically recognizes an epitope in the carboxy terminal part of α-tubulin. It localizes α-tubulin in human, monkey, bovine, chicken, goat, murine, rat, gerbil, hamster, rat kangaroo, amphibia, sea urchin, trypanosome, yeast, fungi and tobacco."

3. anti-S-tag antibodies (Abcam, ab87840) the manufacturer reported the product to work in the following applications: Western Blotting, ELISA. Species reactivity: species independent.

4. anti-ZW10 antibody (Abcam, ab21582): Manufacturer states that the product is suitable for IHC-P, WB, ICC/IF, IP, and that it reacts with Human ZW10. Manufacturer provides numerous references that have used this antibody.

5. Anti-centromere Antibodies (Antibodies, Inc., 15-234-0001): Manufacturer states that "Serum obtained from an autoimmune patient was tested at a series of dilutions by immunocytochemistry on ethanol-fixed Hep2 cells that were in log-phase growth. The staining pattern obtained was consistent with the pattern expected for anti-centromere staining."

6. anti-GFP antibody (Roche, CAT#11814460001): Manufacturer describes the antibody as follows: "Monoclonal antibody for detection of both wild-type and mutant forms of GFP or GFP fusions using: Immunoprecipitation; Western blots; Immunostaining," and provides references for each of these applications. In addition: "Anti-GFP is tested for functionality and purity relative to a reference standard to confirm the quality of each new reagent preparation."

7. Anti-Beta-actin HRP-conjugated (Fisher Scientific, Invitrogen, #MA515739HRP): Manufacturer states that "MA5-15739-HRP has been successfully used in Western blotting applications with human, mouse, rat, rabbit, and chicken samples."

8. Anti-T2A antibody (Sigma-Aldrich, #MABE1923): Manufacturer states that: "A 1:1,000 dilution of this antibody detected T2A tagged alpha-Tubulin in lysate from HEK293 cells transfected with alpha-Tubulin vector."

9. anti-mCherry antibody used for immunoprecipitations was validated in Extended Data Fig. 6G.

10. Other cheeseman lab antibodies were validated in original publications where they were generated, which are referenced in Supplementary Table 2.

Eukaryotic cell lines

Policy information about cell lines and Sex and Gender in Research

Cell line source(s)	All cell lines used in this study are derived from HeLa cells. Generation of specific cell lines was performed as described in methods and Supplementary table 1.
Authentication	Cell lines were not authenticated.
Mycoplasma contamination	Cell lines tested negative for mycoplasma contamination.
Commonly misidentified lines (See ICLAC register)	No commonly misidentified cell lines were used in this study.

Plants

Seed stocks	*Report on the source of all seed stocks or other plant material used. If applicable, state the seed stock centre and catalogue number. If plant specimens were collected from the field, describe the collection location, date and sampling procedures.*
Novel plant genotypes	*Describe the methods by which all novel plant genotypes were produced. This includes those generated by transgenic approaches, gene editing, chemical/radiation-based mutagenesis and hybridization. For transgenic lines, describe the transformation method, the number of independent lines analyzed and the generation upon which experiments were performed. For gene-edited lines, describe the editor used, the endogenous sequence targeted for editing, the targeting guide RNA sequence (if applicable) and how the editor was applied.*
Authentication	*Describe any authentication procedures for each seed stock used or novel genotype generated. Describe any experiments used to assess the effect of a mutation and, where applicable, how potential secondary effects (e.g. second site T-DNA insertions, mosiacism, off-target gene editing) were examined.*

ChIP-seq

Data deposition

☐ Confirm that both raw and final processed data have been deposited in a public database such as GEO.

☐ Confirm that you have deposited or provided access to graph files (e.g. BED files) for the called peaks.

Data access links *May remain private before publication.*	*For "Initial submission" or "Revised version" documents, provide reviewer access links. For your "Final submission" document, provide a link to the deposited data.*
Files in database submission	*Provide a list of all files available in the database submission.*
Genome browser session (e.g. UCSC)	*Provide a link to an anonymized genome browser session for "Initial submission" and "Revised version" documents only, to enable peer review. Write "no longer applicable" for "Final submission" documents.*

Methodology

Replicates	*Describe the experimental replicates, specifying number, type and replicate agreement.*
Sequencing depth	*Describe the sequencing depth for each experiment, providing the total number of reads, uniquely mapped reads, length of reads and whether they were paired- or single-end.*
Antibodies	*Describe the antibodies used for the ChIP-seq experiments; as applicable, provide supplier name, catalog number, clone name, and lot number.*
Peak calling parameters	*Specify the command line program and parameters used for read mapping and peak calling, including the ChIP, control and index files used.*
Data quality	*Describe the methods used to ensure data quality in full detail, including how many peaks are at FDR 5% and above 5-fold enrichment.*
Software	*Describe the software used to collect and analyze the ChIP-seq data. For custom code that has been deposited into a community repository, provide accession details.*

Flow Cytometry

Plots

Confirm that:

☒ The axis labels state the marker and fluorochrome used (e.g. CD4-FITC).

☒ The axis scales are clearly visible. Include numbers along axes only for bottom left plot of group (a 'group' is an analysis of identical markers).

☒ All plots are contour plots with outliers or pseudocolor plots.

☒ A numerical value for number of cells or percentage (with statistics) is provided.

Methodology

Sample preparation	Samples were prepared as described in the methods: Cells were incubated in doxycycline for 24 hours. EDTA, Hoechst-33342 (Sigma-Aldrich), and Verapimil (Tocris; Spirochrome) were added directly to media for 30 minutes to 1 hour to detached cells from the plate and stain them. Cells were collected and filtered through 35 um nylon mesh (Falcon), then run on the flow cytometer.
Instrument	BD Fortessa
Software	BD FACSDiva was used to collect data and FlowJo 9 and 10 were used to analyze the data.
Cell population abundance	N/A
Gating strategy	An example gating strategy is shown in Extended Data Fig. 7. Side Scatter-Area and Forward Scatter-Area were used to gate out dead cells and debris. Forward Scatter-Area and Forward Scatter-Height were used to make a gate for single cells. A gate for the population expressing the constructs at an appropriate expression level was made with GFP-Area and tdTomato-Area for Sun Tag experiments or with a GFP-Area Histogram for I3-01 experiments. Afterwards, we used Hoechst-Area and Hoechst-Width for a secondary gate to exclude aggregates and doublets. Finally, we performed cell cycle analysis on a Hoechst-Area histogram using FlowJo.

☒ Tick this box to confirm that a figure exemplifying the gating strategy is provided in the Supplementary Information.

Magnetic resonance imaging

Experimental design

Design type	*Indicate task or resting state; event-related or block design.*
Design specifications	*Specify the number of blocks, trials or experimental units per session and/or subject, and specify the length of each trial or block (if trials are blocked) and interval between trials.*
Behavioral performance measures	*State number and/or type of variables recorded (e.g. correct button press, response time) and what statistics were used to establish that the subjects were performing the task as expected (e.g. mean, range, and/or standard deviation across subjects).*

Acquisition

Imaging type(s)	*Specify: functional, structural, diffusion, perfusion.*
Field strength	*Specify in Tesla*
Sequence & imaging parameters	*Specify the pulse sequence type (gradient echo, spin echo, etc.), imaging type (EPI, spiral, etc.), field of view, matrix size, slice thickness, orientation and TE/TR/flip angle.*
Area of acquisition	*State whether a whole brain scan was used OR define the area of acquisition, describing how the region was determined.*

Diffusion MRI   ☐ Used   ☐ Not used

Preprocessing

Preprocessing software	*Provide detail on software version and revision number and on specific parameters (model/functions, brain extraction, segmentation, smoothing kernel size, etc.).*
Normalization	*If data were normalized/standardized, describe the approach(es): specify linear or non-linear and define image types used for transformation OR indicate that data were not normalized and explain rationale for lack of normalization.*

Normalization template	*Describe the template used for normalization/transformation, specifying subject space or group standardized space (e.g. original Talairach, MNI305, ICBM152) OR indicate that the data were not normalized.*
Noise and artifact removal	*Describe your procedure(s) for artifact and structured noise removal, specifying motion parameters, tissue signals and physiological signals (heart rate, respiration).*
Volume censoring	*Define your software and/or method and criteria for volume censoring, and state the extent of such censoring.*

Statistical modeling & inference

Model type and settings	*Specify type (mass univariate, multivariate, RSA, predictive, etc.) and describe essential details of the model at the first and second levels (e.g. fixed, random or mixed effects; drift or auto-correlation).*
Effect(s) tested	*Define precise effect in terms of the task or stimulus conditions instead of psychological concepts and indicate whether ANOVA or factorial designs were used.*

Specify type of analysis: ☐ Whole brain   ☐ ROI-based   ☐ Both

Statistic type for inference	*Specify voxel-wise or cluster-wise and report all relevant parameters for cluster-wise methods.*

(See Eklund et al. 2016)

Correction	*Describe the type of correction and how it is obtained for multiple comparisons (e.g. FWE, FDR, permutation or Monte Carlo).*

Models & analysis

n/a	Involved in the study
☐	☐ Functional and/or effective connectivity
☐	☐ Graph analysis
☐	☐ Multivariate modeling or predictive analysis

Functional and/or effective connectivity	*Report the measures of dependence used and the model details (e.g. Pearson correlation, partial correlation, mutual information).*
Graph analysis	*Report the dependent variable and connectivity measure, specifying weighted graph or binarized graph, subject- or group-level, and the global and/or node summaries used (e.g. clustering coefficient, efficiency, etc.).*
Multivariate modeling and predictive analysis	*Specify independent variables, features extraction and dimension reduction, model, training and evaluation metrics.*